# Organs-on-chip: towards therapies for cardiovascular disease using human stem cells

Helden, R.W.J. van

3

# CHAPTER

## Disrupted energetics and contraction in cardiomyocytes with infantile mitochondrial cardiomyopathy

Ruben W.J. van Helden[1], Tessa de Korte[1,2], Sarantos Kostidis[3], Hailiang Mei[4], Roderick C. Slieker[6], Kèvin Knoops[6], Aat A. Mulder[6], Richard P. Davis[1], Martin Giera[3], René de Coo[7,8], Christine L. Mummery[1], Milena Bellin[1,9,10]

[1] Anatomy & Embryology, Leiden University Medical Center, The Netherlands
2 Ncardia, Leiden, the Netherlands
[3] Center for Proteomics & Metabolomics, Leiden University Medical Center, The Netherlands
[4] Sequencing Analysis Support core, Leiden University Medical Center, The Netherlands
[5] Cell and Chemical Biology, Leiden University Medical Center, The Netherlands
[6] The Maastricht Multimodal Molecular Imaging Institute, Maastricht University, The Netherlands.
[7] Dept. of Neurology, Erasmus MC University Medical Centre, Rotterdam, The Netherlands
[8] Dept. of Toxicogenomics, Maastricht University, Maastricht, The Netherlands
[9] Department of Biology, University of Padova, Padova, Italy
[10] Veneto Institute of Molecular Medicine, Padova, Italy

# ABSTRACT

Infantile mitochondrial cardiomyopathy causes death shortly after birth. We used human-induced pluripotent stem cells derived cardiomyocytes (hiPSC-CMs) from siblings carrying two compound mutations in the nuclear-encoded mitochondrial-Alanine-tRNA synthetase 2 gene (*AARS2)* to investigate the cardiac pathology. We analysed the structural, metabolic, and functional properties of patient hiPSC-CMs and compared them with familial and gene-corrected controls. The patient's hiPSC-CMs displayed reduced energetic capacity in both oxidative phosphorylation and glycolysis, resulting in reduced ATP production. However, an increase in mitochondrial copy number was identified as a possible compensatory mechanism. Quantitative metabolomics and RNA-sequencing supported metabolic dysregulation, showing less intracellular $NAD^+$ and failure to produce $NAD^+$ from pyruvate. Additionally, we found alternative use of lipids and lipid precursors and a dependency on extracellular aspartate. Finally, *AARS2* mutations caused dysregulation in calcium handling and cardiac ion channel balance, causing arrhythmia and contractile defects. Surprisingly, the patient hiPSC-CMs showed reduced sensitivity to pro-arrhythmic drugs. In conclusion, we captured the pathological features related to infantile mitochondrial cardiomyopathy showing a valuable resource for studying the disease pathology and ways to rescue the phenotype.


**Keywords:** hiPSC-derived cardiomyocytes/Infantile cardiomyopathy/metabolomics/mitochondrial cardiomyopathy/mitochondrial disease model

# INTRODUCTION



Mitochondrial diseases can lead to a variety of pathologies in different human organs (Gorman *et al.,* 2016; Vafai & Mootha, 2012; Koopman *et al.,* 2012). Since mitochondria crucially regulate cell metabolism, it is not surprising that the heart, which has a high energetic demand due to its contractile work, is among the most affected by mitochondrial dysfunction and disease. Mitochondrial diseases are often caused by genetic mutations in either the mitochondrial or nuclear DNA (mtDNA and nDNA, respectively), affecting proteins involved in mitochondrial function (Finsterer & Kothari, 2014). One particular mitochondrial disease is the rare, autosomal recessive combined oxidative phosphorylation deficiency 8 (COXPD8, OMIM: 614096), which leads to lethal infantile cardiomyopathy shortly after birth (Götz *et al.,* 2011). The disease is caused by mutations in the nuclear gene alanyl-tRNA-synthetase 2 (*AARS2)* that encodes the mitochondrial protein alanine-tRNA synthetase (mt-AlaRS). This enzyme plays a crucial role in the protein translation machinery of mitochondria, charging the naïve mitochondrial transfer-RNA$^{Ala}$ with alanine to create alanyl-tRNA while also playing an essential role in verifying the correct charge on other aminoacyl-tRNAs (Euro *et al.,* 2015; Aibara *et al.,* 2020; Sokabe *et al.,* 2009; Guo *et al.,* 2009; Hilander *et al.,* 2018). The role of mitochondrial translation is relatively small, with the mtDNA only encoding 22 tRNAs, 2 ribosomal-RNAs and 13 protein-coding genes (Vafai & Mootha, 2012; Koopman *et al.,* 2012; Anderson *et al.,* 1981). However, these 13 proteins form essential parts of the respiratory chain complexes I, III, IV and V, while complex II is composed solely of subunits encoded in the nDNA. The respiratory chain complexes I-IV are the central drivers of oxidative phosphorylation (OXPHOS), performing the reduction and oxidative (redox) reactions of Nicotinamide-adenine-dinucleotide (NADH) and Flavine-adenine-dinucleotide ($FADH_2$). These reactions create and maintain the proton gradient essential in driving the $F_1F_0$-ATPase complex V, the final OXPHOS step, and charge ADP with an additional phosphate group to ATP. Mutations in *AARS2*, therefore, contribute to translational defects in these 13 subunits, with the misincorporation of amino acids leading to decreased stability of the OXPHOS complexes I, III, IV and V and a lower abundance of fully assembled complexes (Watanabe, 2010; Hilander *et al.,* 2018).

Previous studies have shown that mutations in *AARS2* can lead to either neurological pathologies, known as (ovario)leukodystrophy, or to early-onset lethal infantile cardiomyopathy, depending on the mutational burden (Dallabona *et al.,* 2014; Euro *et al.,* 2015; Taylor *et al.,* 2014; Tang *et al.,* 2019; Sommerville *et al.,* 2019; Götz *et al.,* 2011; Zhang *et al.,* 2022). Similar to other mt-Aminoacyl-tRNA-related pathologies (Watanabe, 2010; Yao & Fox, 2013; Nguyen *et al.,* 2021) and mitochondrial defects in general, the tissue or organ affected depends on which gene is mutated or even the specific genetic mutation (Koopman *et al.,* 2012; Nguyen *et al.,* 2021; Yaplito-Lee *et al.,* 2007; Nielsen *et al.,* 2020). In COXPD8, the *AARS2 c.1774C>T* mutation is recognised as a central mutation leading to infantile cardiomyopathy, either as a homozygous mutation or accompanied by an additional defective

allele with another compound mutations (Götz *et al.,* 2011; Sommerville *et al.,* 2019; Mazurova *et al.,* 2016). While the disease is very rare, the pathology observed in patients is well described. Pathological features common to all COXP8 patients include (hypertrophic) cardiomyopathy, cytochrome oxidase (COX) negative muscle fibres, reduced expression of the OXPHOS complexes I, III, IV and V in both heart and muscle fibres, and lactic acidosis, in addition to a varying degree of neurological pathology. However, few studies to date have examined the characteristics of the mutations in detail and compared this directly with functional features of affected cells such as cardiomyocytes.

Human-induced pluripotent stem cells (hiPSCs) offer an opportunity to model mitochondrial cardiomyopathies, explore the underlying pathological molecular mechanisms and test therapeutic options (Pavez-Giani & Cyganek, 2022). Indeed, mitochondrial cardiomyopathies due to nDNA mutations, mainly with hypertrophic and dilated phenotypes, have previously been modelled using cardiomyocytes differentiated from hiPSCs (hiPSC-CMs). These studies include research into pathologies such as Leigh syndrome (Hallas *et al.,* 2018), Friedreich's ataxia (Hick *et al.,* 2013; Wong *et al.,* 2019; Lee *et al.,* 2016; Li *et al.,* 2019), Barth syndrome (Wang *et al.,* 2014; Jin *et al.,* 2016; Fatica *et al.,* 2019; Dudek *et al.,* 2016; Chowdhury *et al.,* 2018), dilated cardiomyopathy with ataxia (Rohani *et al.,* 2020), and very long-chain acyl-coenzyme A dehydrogenase deficiency (Knottnerus *et al.,* 2020). These studies using hiPSC-CMs, either in 2-dimensional culture or engineered heart constructs, have revealed ultrastructural abnormalities of the mitochondria, reduced oxidative capacity, aberrant calcium handling and electrophysiological properties, and impaired force of contraction. However, so far, no hiPSC-based cardiac models have been reported for *AARS2* mutations with prominent infantile cardiomyopathy phenotype, possibly due to the fatal and early onset (perinatal to early post-natal) disease phenotype leading to difficulties in obtaining primary material (Mazurova *et al.,* 2016).

Here, we studied cardiomyocytes differentiated from hiPSCs generated from newborn-sibling patients carrying compound mutations in *AARS2* and their apparently healthy mother who carried one heterozygous *AARS2* mutation (van Helden *et al.,* 2021). We also created genetically corrected hiPSC controls matching the unaffected father's genotype. In the patient hiPSC-CMs, mitochondrial dynamics were disrupted, and metabolic homeostasis was altered, reducing ATP and altering the usage of amino acids and lipids. These changes led to dysregulation in calcium handling and electrophysiological properties, resulting in arrhythmic behaviour and altered contractility kinetics. The results in this study provide insights into *AARS2* mutation effects on hiPSC-CM function and could ultimately help identify targets for therapy.

# RESULTS

## Generation of isogenic pairs of hiPSC lines from patients with COXPD8 and their differentiation into cardiomyocytes

Three siblings, male twins and another brother, presented with circulatory and respiratory insufficiency shortly after birth (Kamps *et al.,* 2018). Fig. 1A shows the family tree, where patient 1 (II-1) showed hypertrophic cardiomyopathy and additional signs of hypotonia and convulsions with persistent lactic acidosis. The patient died five days postpartum. Patient 2 (II-3) was diagnosed with hypertrophic cardiomyopathy shortly after birth, presented with lactic acidosis and died several days postpartum. Genetic testing by exome sequencing revealed two compound mutations in the *AARS2* gene, c.1774C>T inherited via the father's allele and c.2872C>T present on the mother's allele (Fig. 1A, B) (Kamps *et al.,* 2018). The c.1774C>T missense mutation is associated with the COXPD8 pathology when present homozygously or in conjunction with a pathological compound mutation on the other allele (Taylor *et al.,* 2014; Sommerville *et al.,* 2019). The c.2872C>T nonsense mutation, which has not been described in other patients before, is present in the gene's last exon, resulting in protein truncation. For our study, hiPSCs from the two patients carrying the compound mutations, brothers both from different pregnancies (II-1 and II-3), and their mother, carrying the heterozygous truncation (I-2) were available (Fig. 1A, LUMCi024-A, LUMCi025-A and LUMCi026-A, respectively and as described previously (van Helden *et al.,* 2021), hereafter refered to as Pt 1, Pt 2 and Ctrl).

We designed a gRNA to correct the c.2872C>T mutation using CRISPR/Cas9 technology to create isogenic control hiPSC lines from Pt 1 and Pt 2 that matched the father's genotype (Fig. S1A and table S1). By using ddPCR for screening, we simultaneously detected the wild-type- (WT), mutant- and corrected alleles (Fig S1A, B). Three clones from Pt 1 and two from Pt 2 were isolated (3/82 and 2/89), with a correction efficiency of 2.8% (Fig. S1C). Further characterisation of the clones confirmed correction of the mutation and the introduction of the three silent mutations (Fig. 1C, Fig. S1F). All corrected clones showed normal karyotypes by G-banding and expressed the pluripotency markers OCT3/4, SSEA4, and NANOG (Fig. S1D, E), similar to the respective parental lines (van Helden *et al.,* 2021). We selected one corrected clone per line, hereafter refered to as Iso 1 and Iso 2 (LUMCi024-A-corrected and LUMCi025-A-corrected on hPSCreg) for further characterisation and used the following nomenclature throughout the manuscript: LUMCi024-A and LUMCi025-A are patient 1 (Pt 1) and patient 2 (Pt 2), respectively, LUMCi024-A-corrected and LUMCi025-A-corrected are Iso 1 and Iso 2, respectively; LUMCi026-A is the control (Ctrl).

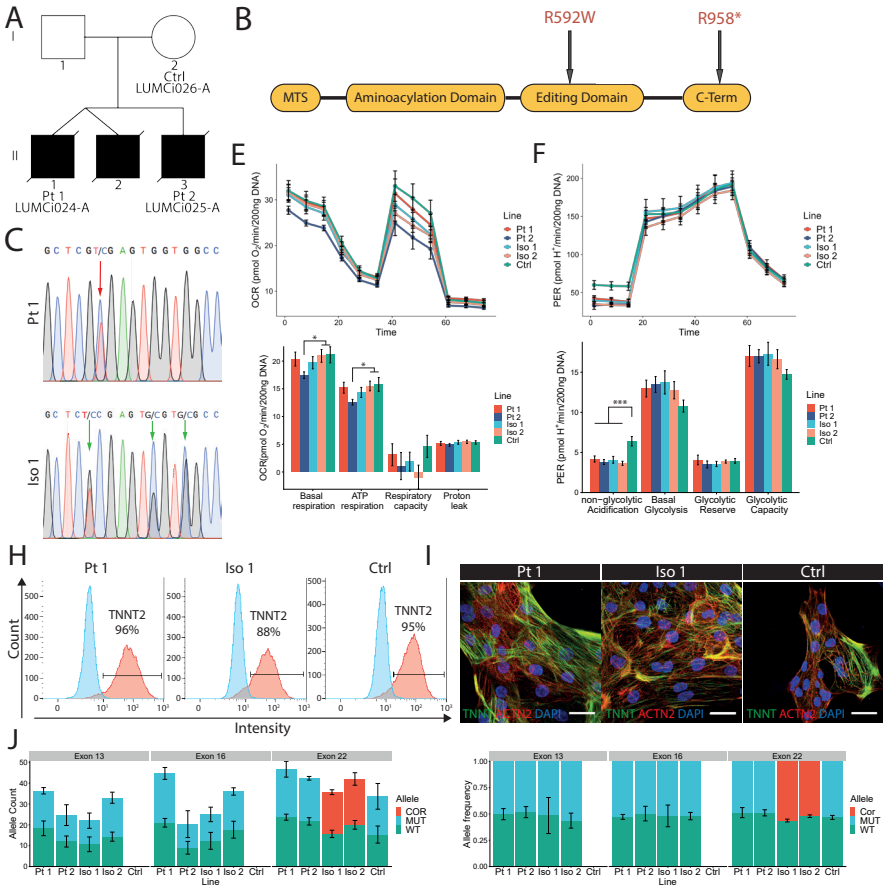


***Figure 1: genealogy, genetic correction in hiPSCs, metabolic characterisation of hiPSCs and differentiation into cardiomyocytes.***

A) Genealogy showing unaffected (white) and affected individuals (black). Circle: female; square: male. The hiPSC lines were generated from the unaffected mother (I-2, LUMCi026-A or Ctrl), and two affected children (II-1 and II-3, LUMCi024-A or Pt 1, and LUMCi025-A or Pt 2, respectively). B) Graphical representation of the enzyme Mt-AlaRS with the different protein domains. The locations of the two pathological amino acid mutations, R592W and R958*, are shown in red, and the additional polymorphism V730M is indicated in a lighter shade. C) Sanger sequencing chromatogram of DNA isolated from Pt 1 and Iso 1 hiPSCs showing the corrected c.2872C>T mutation in Iso 1. D and E) Traces of extra-cellular flux assays in undifferentiated hiPSCs by Seahorse measuring Oxygen consumption rate (OCR) (D) and proton extrusion rate (PER) (E). Below is the quantification of the different processes (basal respiration, ATP respiration, respiratory capacity, proton leak, (E, bottom) and non-glycolytic acidification, basal glycolysis, glycolytic reserve, and glycolytic capacity (F, bottom)) is shown as a bar graph. N ≥ 18, n = 3 biological repeats, data represented as mean and standard error. F) Cardiomyocyte differentiation protocol. Day 0 (D 0) was defined as the first induction of the mesoderm. BMP 4: Bone morphogenetic protein 4; CHIR = CHIR99021; XAV: XAV-939. Lactate treatment was used as metabolic selection for enriching the cardiomyocyte population. G) Representative FACS measurement (histograms) for cardiac troponin T (TNNT) (red) in Pt 1, Iso 1, and Ctrl hiPSC-CMs after lactate selection. Cells stained with isotype-matched antibodies were used as a negative control in blue. H) Representative immunofluorescence images of cardiac sarcomeric proteins TNNT (green) and α-actinin 2 (ACTN2, red) in Pt 1, Iso 1, and Ctrl hiPSC-CMs. Nuclei are stained in blue with DAPI. Scale bar = 25 µm. I) AARS2 allelic expression quantification from RNA-sequencing showing the copy number for WT (green),

mutated (blue), and corrected (red) alleles. Left panel: absolute count; right panel: allele frequency. N = 3 biological repeats. Error bar: standard error. Statistics are indicated as follows unless otherwise indicated. * P < 0.05, ** P < 0.01, *** P < 0.001 with student's t-test.



An unregular cellular phenotype was observed during the culture of the patient and isogenic hiPSC lines. Massive cell death would occur when these lines were allowed to grow at confluencies higher than 80%. This behaviour, however, was not apparent in the Ctrl line. Higher basal rates of glycolysis and lower rates of OXPHOS could be depleting glucose more rapidly in the medium, resulting in this observed phenotype. We performed Seahorse extra-cellular flux measurements to uncover whether metabolic differences were already present in the undifferentiated hiPSCs. These measurements revealed that Pt 2 had lower basal respiration and ATP-coupled respiration compared to Iso 2 and the Ctrl (fig. 1E.), but the other lines did not show any differences in respiration. Measuring glycolysis, we observed that both the Pt and Iso lines had a lower non-glycolytic acidification rate compared to Ctrl, suggesting a lower total contribution to glycolysis (Fig. 1F), however, this did not result in a significantly lower basal glycolytic rate.

We modified the differentiation protocol by shortening the mesoderm induction period from 3 to 2 days and adjusted the concentration of the growth factors Activin A and BMP4 per line (Fig. 1G). This led to >85% hiPSC-CMs in differentiated populations after lactate selection as determined by flow cytometric analysis for cardiac troponin T (TNNT2) for all five lines (Fig. 1H, Fig. S1J). The hiPSC-CMs showed typical sarcomere organisation, independent of whether they were Pt, Iso, or Ctrl (Fig. 1I, Fig. S1K). Finally, whole-genome gene expression by RNA sequencing (RNA-seq) revealed similar *AARS2* allele frequencies in all the lines, suggesting that the *AARS2* mutations and correction of c.2872C>T did not affect either allele expression or mRNA stability (Fig. 1J).

## Patient hiPSC-CMs have altered mitochondrial function

The *AARS2* mutations lead to decreased mitochondrial OXPHOS complexes I, III, IV and V in cardiac biopsies from patients, as well as lactic acidosis in their blood plasma (Kamps *et al.,* 2018). To assess the mitochondrial properties of our hiPSC-CMs, mitochondrial OXPHOS complexes and the protein mt-AlaRS were quantified by Western blot. We found reduced mt-AlaRS expression compared to both the corresponding Iso and Ctrl hiPSC-CMs, and reduced complex IV mitochondrially encoded cytochrome c oxidase I (MTCO1) in Pt 1 when compared to Iso 1 (Fig. 2A,B, Fig. S2A,B, Fig. S3A,B). Additionally, the mitochondrial household gene and loading control, Voltage-dependent anion-selective channel 1 (VDAC1), was unchanged (Fig. S2C, Fig. S3C) when normalised to the whole cell lysate, indicating no differences in mitochondrial biogenesis. Strikingly, we found that the copy number of mtDNA per cell was increased in the patient hiPSC-CMs versus the isogenic

controls, with the maternal control showing even lower numbers than the corrected control (Fig. 2C, Fig S3D). TEM was used to examine mitochondrial ultrastructure (Fig. 2D, Fig. S3E), which did not differ between hiPSC-CMs from all lines. Finally, mitochondrial membrane potential (MMP) and network organisation were assessed using TMRM (Fig. S2D). Both MMP, expressed here as mean mitochondrial intensity, and the mean mitochondrial volume was increased in the patients compared to their isogenic controls and Ctrl (Fig. 2E, Fig. S3F).

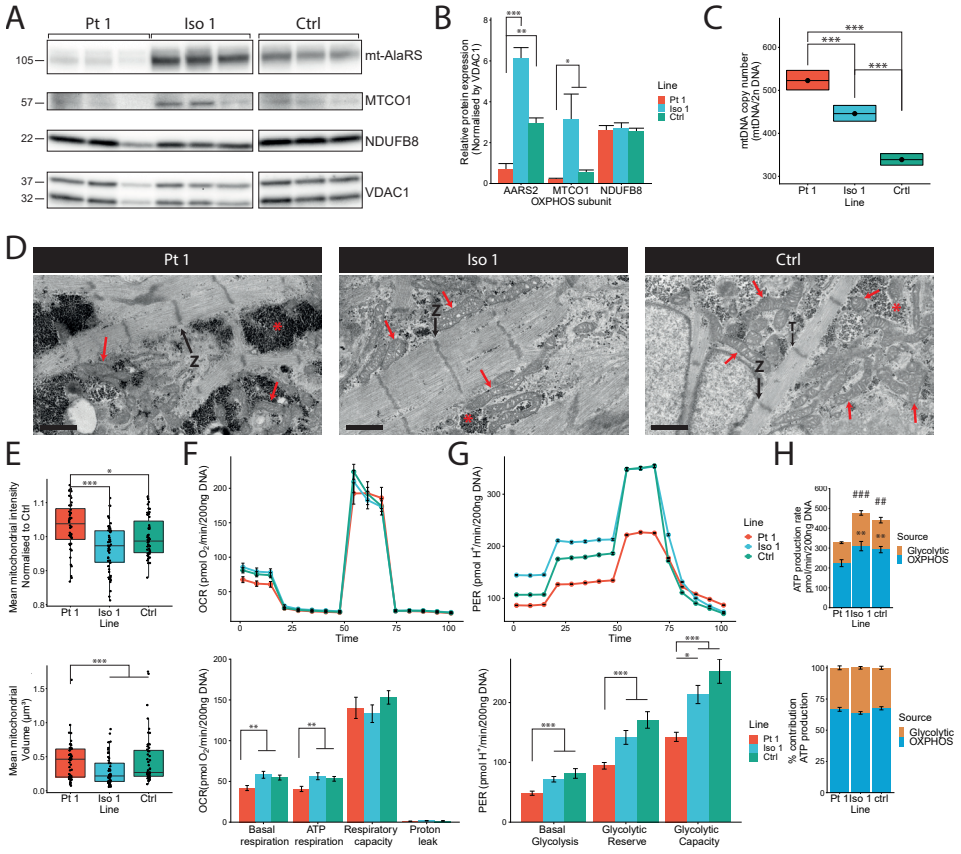


***Figure 2: Altered mitochondrial protein expression, mitochondrial organisation and metabolic flux in Pt 1 hiPSC-CMs.***

A) Western blot showing expression of mitochondrial proteins mt-AlaRS, MTCO1, NDUFB8, and VDAC1 in Pt 1, Iso 1 and Ctrl hiPSC-CMs. Each column represents an independent differentiation (biological replicate). B) Quantification of mitochondrial protein expression, normalised by VDAC1 expression as a marker for total mitochondrial biomass. C) mtDNA copy number per cell, quantified by ddPCR. The plot represents the Poisson minimum, mean, and maximum number of mtDNA per 2N nDNA copy number. Calculations based on Poisson distribution. N =22-26, n = 3-4 biological repeat, ** P < 0.01, *** P < 0.001, Poisson statistics. D) Representative transmission electron microscopy (TEM) images from Pt 1, Iso 1, and Ctrl hiPSC-CMs. The red arrow indicates mitochondria, the red star indicates glycogen deposits and black Z the Z-disk. Scale bar = 1 µm. E) Quantification

of the intensity of the TMRM dye in mitochondria, normalised to the mean of the Ctrl and mean volume of each identified mitochondria. Each dot represents the mean value obtained per microscope field. N = 12, n = 1 biological repeat. F and G) Traces of extra-cellular flux assays in hiPSC-CMs by Seahorse measuring Oxygen consumption rate (OCR) (F) and proton extrusion rate (PER) (G). At the bottom of each panel, quantification of the different processes (basal respiration, ATP respiration, Respiratory capacity, proton leak, (F, bottom) and basal glycolysis, glycolytic reserve, and glycolytic capacity (G, bottom)) is shown as a bar graph. N ≥ 18, n = 3-4 biological repeats. H) Total ATP production (top) and contribution of OXPHOS and glycolysis to total ATP production (bottom), calculated based on extra-cellular flux measurements. Statistical differences are denoted in comparison to Pt 1. # marks statistical differences when comparing Glycolytic ATP production rate: ## P < 0.01, ### P < 0.001, and * for the OXPHOS ATP production rate ** P < 0.01. N ≥ 18, n = 3-4 biological repeats. All data shown are mean with standard error and are n = 3 biological repeats unless otherwise stated. Statistics are indicated as follows unless otherwise indicated. * P < 0.05, ** P < 0.01, *** P < 0.001 with student's t-test.



In contrast to the increase in MMP and mtDNA copy number, mitochondrial respiration was reduced in the patient hiPSC-CMs compared to the Iso and Ctrl hiPSC-CMs, with lower OCR during basal ATP generation, and additionally, a lower spare respiratory capacity in Pt 2 compared to Iso 2 (Fig. 2F, Fig. S3G). Glycolysis was also reduced in the patient hiPSC-CMs, with lower glycolytic capacity and glycolytic reserve, and an additional reduced basal glycolytic activity in Pt 1 compared to Iso 1 (Fig. 2G, Fig. S3H). Together, this resulted in an overall reduction of 30% in oxidative and glycolytic ATP production rates in both the patient hiPSC-CMs compared with the controls, while the relative contribution of both pathways remained the same between Pt 1 and Iso 1 and had a higher reliance on glycolysis in Pt 2 compared to Iso 2 (Fig. 2H, Fig. S3I).

Altogether, these results showed that patient hiPSC-CM mitochondria had altered structure and function compared with controls.

## Altered central carbon and lipid metabolism, as well as gene expression in patient hiPSC-CMs

Quantitative metabolomics of hiPSC-CMs and the exchange of metabolites with the culture medium revealed reduced intracellular concentrations of several amino acids and energy-carrying substrates such as ATP, $NAD^+$ and creatine phosphate in Pt 1 when compared to Iso 1 or Ctrl, as well as reduced concentrations of key lipid precursors acetate, choline, glycerol, and sn-Glycero-3-phosphocholine and increased concentration of O-phosphocholine in Pt 1 compared to Iso 1 hiPSC-CMs, with the Ctrl showing the highest levels among the samples (Fig. 3A). Pt 2 showed a similar profile, with reduced energy-carrying substrates, notably ATP, GTP, $NAD^+$ and lactate, with the exception of creatine. The lipid precursor profile was less clear, with decreased concentrations of acetate and sn-Glycero-3-phosphocholine, but with increased cholone, o-phosphocholine and glycerol (fig. S4A). Quantitative lipidomics revealed higher lipid concentrations in Ctrl compared with both Iso 1 and Pt 1 hiPSC-CMs (Fig. 3B, Table S3).

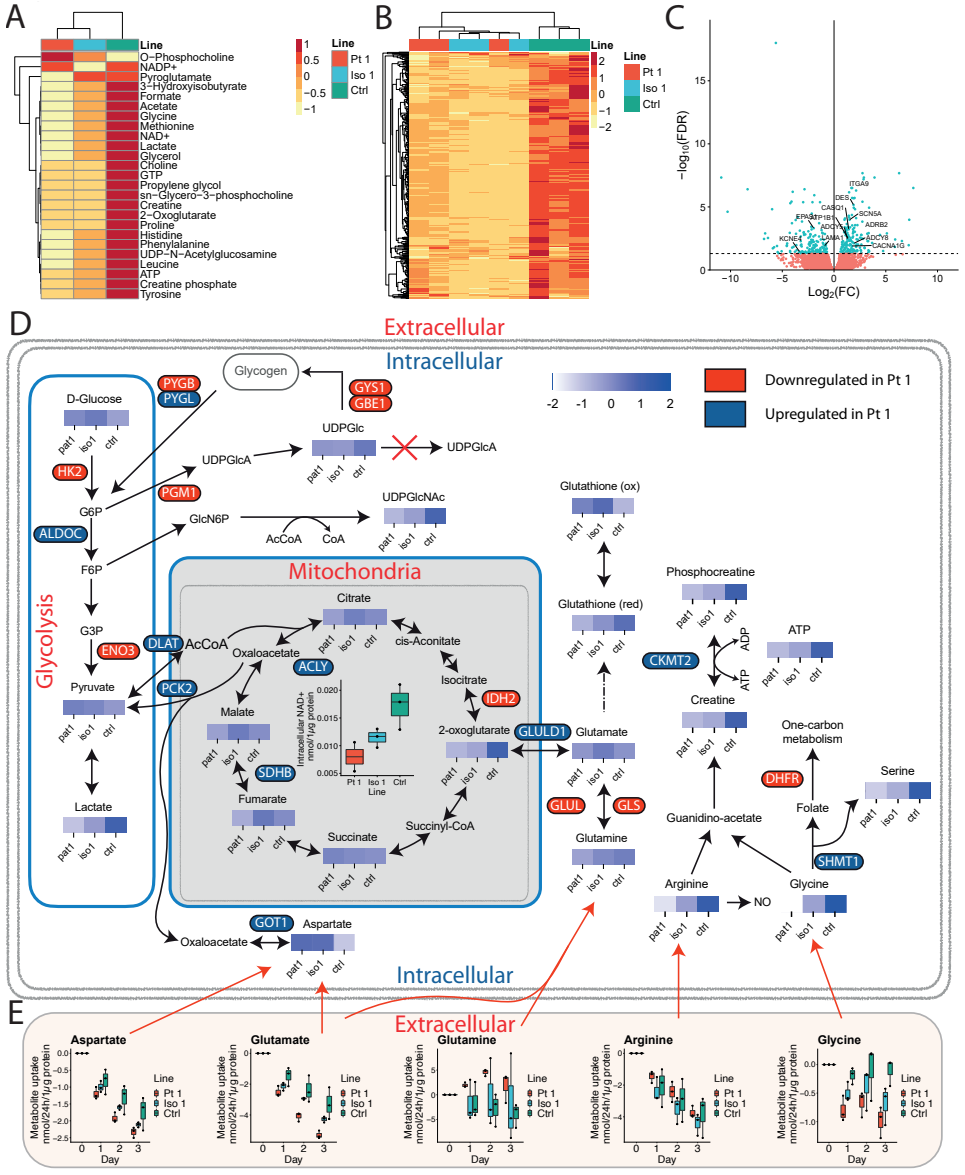


***Figure 3. Metabolomic and transcriptomic analysis shows altered metabolic pathways utilisation in Pt 1 hiPSC-CMs.***

A) Hierarchical clustering based on intracellular metabolites quantified by NMR (nuclear magnetic resonance); n = 2-3 biological repeats. The scale represents Z-score. B) Hierarchical clustering based on all detected lipids on the Lipidyzer platform; n = 3. The scale represents Z-score. C) Volcano plot showing the distribution of all genes detected by RNA-sequencing, in blue genes equal to or lower than the 5% false-discovery rate. The marked genes are subselections of genes related to hypertrophy and cardiac development. D) Combined pathway analysis of intracellular metabolites; upregulated genes (blue) and downregulated (red) genes in Pt 1 versus Iso 1 and Ctrl hiPSC-CMs are visualised (p.value < 0.15 and 20% altered fold-change). E) Metabolite exchange from the medium.

Transcriptomic analysis indicated that 44% of the variance in the data could be explained by principal components 1 and 2, resulting in the separation of Pt 1 from Iso 1 and Ctrl but closer alignment between Pt 2 and Iso 2 (Fig. S4B, C). Analysis of differentially expressed genes (DEGs) identified a total of 689 DEGs across three sets of analyses, with 368 DEGs detected when comparing Pt 1 hiPSC-CMs with Iso 1 hiPSC-CMs, 335 DEGs between Pt 1 and Ctrl, and 361 DEGs when comparing Pt 1 with the "healthy" lines (Pt 1 vs Iso 1 and Ctrl, with correction of genetic background, Fig. S4D). Hierarchical clustering based on the 361 DEGs from Pt 1 vs healthy lines showed that the Pt 1 hiPSC-CMs clustered separately from both the Iso 1 and Ctrl CMs, driven mainly by differences between Pt 1 and Iso 1 (Fig. S4E). Finally, hierarchical clustering on the 42 DEGs generated by comparing the patients to both isogenic lines showed different gene expression clusters between the patient lines versus isogenic and control lines (Fig. S4F), indicating the presence of the *AARS2* mutations does influence general gene expression in hiPSC-CMs.

Pathway analysis combining intracellular metabolite concentrations, their exchange with the growth medium and gene expression indicated key differences between Pt 1 and the Iso 1 and Ctrl hiPSC-CMs (Fig. 3D and 3E). In particular, and in agreement with the Seahorse assay, Pt 1 and Pt 2 cells produced less lactate. However, a more detailed analysis of the data pointed to differences in mitochondrial metabolism, redox balance, substrates for energy generation and links to lipogenesis/lipolysis. The data also highlighted the following: i) the upregulation of dihydrolipoamide S-acetyltransferase (*DLAT*) in Pt 1 combined with reduced lactate production suggests that most of the intracellular pyruvate is transferred into the mitochondria and converted to AcCoA and subsequently to citrate, ii) decreased 2-oxoglutarate in Pt 1 combined with the downregulation of Isocitrate dehydrogenase (*IDH2*), indicates the reduced oxidative conversion of citrate to 2-oxoglutarate. iii) lower $NAD^+$ in Pt 1 and Pt 2 as a result of impaired respiration (mitochondrial $NAD^+$) and reduced conversion of pyruvate to lactate (production of cytosolic $NAD^+$), further verified by additional independent measurements of intracellular $NAD^+$ in both patients (Fig. S4G). iv) higher intracellular aspartate in Pt 1 and Iso 1, and a significantly higher influx of extra-cellular aspartate in Pt 1 combined with upregulation of cytosolic glutamic-oxaloacetic transaminase 1 (*GOT1*) to facilitate aspartate *de novo* synthesis from oxalacetate. v) a higher influx of extra-cellular glutamate in Pt 1 combined with upregulated glutamate dehydrogenase 1 (*GLULD1*) and with downregulation of glutamate-ammonia ligase (*GLUL)* and glutaminase (*GLS*), additionally identified as altered regulation in the mitochondrial pathway analysis in both Pt 1 and Pt 2. These data suggest that Pt 1 cells preferentially utilise extra-cellular glutamate rather than from glutaminolysis, which in turn can be converted to 2-oxoglutarate in an $NAD^+$-dependent step. vi) the upregulation of ATP citrate lyase (*ACLY*) in Pt 1, suggesting conversion of cytosolic citrate, which can be generated from either reductive carboxylation of glutamine and/or from pyruvate entering the TCA via AcCoA to cytosolic oxalacetate. vii) Pt 1

cells exhibited more oxidised and less reduced glutathione suggesting differences in ROS production. viii) Pt 1 and Pt 2 had lowered intra-cellular glycine, and Pt 1 also showed increased consumption of extra-cellular glycine. This altered glycine concentrations, combined with the upregulation of serine hydroxymethyltransferase 1 (*SHMT1*) and downregulation of dihydrofolate reductase 2 (*DHFR*), might also contribute to higher serine biosynthesis and utilisation in Pt 1 rather than contributing one-carbon units to the folate pathway. Interestingly, these pathways were also found to be altered in regulation according to the MitoCarta3 dataset (Fig. S4H). ix) While overall, Pt 1 exhibited lower pools of high energy phosphates (ATP, phosphocreatine), the upregulation of mitochondrial creatine kinase 2 (*CKMT2*) could indicate consumption of extra-cellular glycine by Pt 1 to produce phosphocreatine. x) Choline and ethanolamine pathways were also different in Pt 1, including the phosphorylation to phosphocholine (PCho) and phosphoethanolamine (PEtn), as well as the levels of formed *sn*-glycerophosphocholine (GPC). Interestingly, the expression of enzymes degrading PC into GPC, as well as those that convert PEtn to acetate and AcCoA, were all increased in Pt 1 (Fig. S4I). xi) In addition to the overall lower levels of all lipids classes in Pt 1 (Fig. 3B), we also observed lower intracellular free glycerol – a source of the three-carbon backbone of TAG and other lipids. This lower free glycerol combined with increased uptake of glycerol from the medium in Pt 1 and Iso 1, lower lipoprotein lipase (*LPL*) (degradation of lipids to free glycerol) and higher glycerol kinase (*GK5*) (conversion of glycerol to glycerol-3-phosphate to facilitate the production of pyruvate), matched by lower expression of glycerol-3-phosphate dehydrogenase 1 like enzyme (*GPD1L*) (conversion of dihydroxyacetone phosphate to glycerol-3-phosphate, away from glycolysis) in Pt 1 (Fig. S4I). Combining all glycerol-related and PE/PC-related data suggests different capacities of Pt 1 for lipid synthesis and utilisation of lipolysis products, albeit these links need further investigation.

Mitochondrial pathways were analysed using MitoCarta3 by performing four comparisons; Pt 1 vs Iso 1, Pt 2 vs Iso 2, both patients vs both isogenic, correcting for genetic background and finally, both patients vs the isogenic and the Ctrl line, again correcting for genetic background. This pathway analysis revealed some consensus (Fig. S4H). Specifically, genes related to mtRNA regulation and ribosome seemed to be affected in both Pt 1 and Pt 2. Furthermore, glutamate, glycine and 1-carbon metabolism were found to be altered in regulation, compounding the observations made with the metabolomics analysis.

Further analysis of the RNA-seq using KEGG also revealed several altered pathways related to metabolic homeostasis, contractile apparatus or adhesion molecules, calcium handling, and translation and transcription (Fig. 4A). Additionally, GO-term analysis revealed altered transport and phosphorus metabolism pathways (Fig. 4B).

## Calcium transients in patient hiPSC-CMs showed altered dynamics and arrhythmic behaviour

We were particularly interested in investigating whether the observed transcriptional differences in calcium handling and contraction pathways were paralleled by functional consequences, as calcium dynamics play an essential role in the excitation-contraction coupling of cardiomyocytes. Therefore, we measured the calcium transients and contraction profiles of the patient and control hiPSC-CMs. The cardiomyocytes from each of the hiPSC lines displayed a range of different calcium transient profiles, with some wells showing typical, rhythmic calcium traces and other wells presenting arrhythmic calcium transients (Fig. 4C, D). The arrhythmic behaviour was analysed by plotting the data in Poincaré plots. In Pt 1 hiPSC-CMs, the Poincaré profile showed a greater spread and quantification showed a larger standard deviation along the intersecting line, indicating a higher incidence of arrhythmic transients than the Iso 1 and Ctrl hiPSC-CMs (Fig. 4E, F).

Quantifying the calcium transient characteristics during non-arrhythmic transients revealed prolonged peak-to-peak-intervals (PtP-intervals) under spontaneous beating, with subsequent increases in the calcium-transient duration at 90% decay and calcium amplitude in Pt 1 compared to Iso 1 and Ctrl (Fig. S5A). Additionally, both the rising- and decay-slope were decreased, in line with an increase in rising and decay time in Pt 1 compared to Iso 1 and Ctrl CMs (Fig. S5A). We used caffeine, a Ryanodine Receptor 2 (RYR2) channel agonist, to induce calcium release from the sarcoplasmic reticulum (SR) and measure total cytosolic calcium. The addition of caffeine prolonged peak duration and increased amplitude in the Ctrl compared to both Pt 1 and Iso 1 hiPSC-CMs, while the peak area did not differ between the lines (Fig. S5B, C). These results suggest that the observed calcium changes between Pt 1 and Iso 1 were not due to differences in total cytosolic calcium.

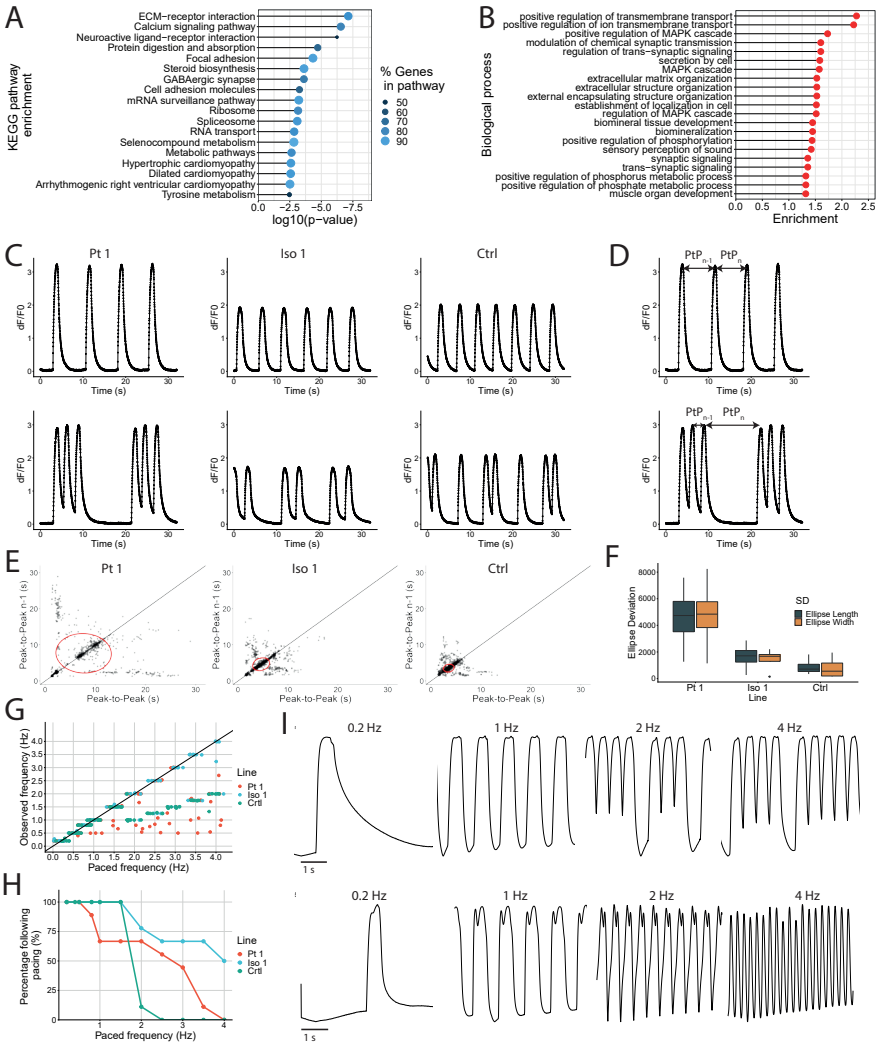


***Figure 4. Altered calcium homeostasis and arrhythmic behaviour Pt 1 in hiPSC-CMs.***

A) KEGG pathways were found altered in their expression. (FDR adjusted p-value < 0.05). B) Gene-ontology (GO) biological processes analysis of enriched pathways (Kruskal-Wallis p-value < 0.05). C) Representative calcium transient traces showing rhythmic calcium profiles (top) and arrhythmic calcium profiles (bottom) in spontaneously contracting hiPSC-CMs. D) Graphs showing the method for calculating the poincaré plots from rhythmic (top) and arrhythmic (bottom) calcium traces; each peak-to-peak (PtP) time as compared to the previous peak. E) Poincaré plots showing arrhythmia, marked as a red ellipse drawn based on calculating standard deviation along and perpendicular to the dissecting line (N = 60, n = 4 biological repeats). F) Quantification of the ellipse statistics. G) Ability of hiPSC-CMs to follow increasing pacing frequencies. The x-axis shows paced frequency. The y-axis shows the observed beating rate of the hiPSC-CMs. All data points underneath the intersecting line reflect hiPSC-CMs not contracting at the paced frequency. (N = 8-9, n = 3 biological repeats). H) Representative traces show different contractile characteristics during ramped pacing. Pt 1 hiPSC-CMs (top) show arrhythmic contractile properties at higher frequencies, while Iso 1 hiPSC-CMs (bottom) retain regular beating intervals. I) Quantification of the percentage of samples able to follow the paced frequency up to 4 Hz.

We then measured the contraction characteristics of the hiPSC-CMs. In agreement with the calcium transient analysis, Pt 1 hiPSC-CMs showed a higher spontaneous Beat-to-Beat (BtB) rate, higher contraction duration and increased relaxation time compared to Iso 1 and Ctrl, while time-to-peak was unchanged (Fig. S5D). To mimic physiologically relevant beat-rates and the cellular stress induced by high beat rates, we paced the hiPSC-CMs at increasing frequencies, starting from 0.2 Hz and ramping up to 4 Hz (Fig. 4G). From 0.8 Hz onwards, both the patient hiPSC-CMs showed diminished capability to follow the increased pacing frequencies compared to their corresponding isogenic CMs (Fig. 4G, H). Additionally, when the patient hiPSC-CMs failed to follow the paced frequency, both lines showed an arrhythmic behaviour (Fig. 4I). Conversely and, different to the isogenic CMs that were able to respond to all the pacing frequencies, the Ctrl hiPSC-CMs could not be paced above 2 Hz. Instead, they reliably contracted at half of the pacing frequency, resulting in beat rates of 1, 1.5 and 2 Hz while paced at 2, 3 and 4 Hz, respectively. Although Pt 2-hiPSC-CMs did not differ from Iso 2 in calcium handling (Fig. S6A-E), the contraction duration and time-to-peak were both increased in Pt 2 (Fig. S6F). Additionally, Pt 2 showed the same high prevalence of arrhythmias as Iso 2 (Fig. S6G-H). These results indicated that the patient-derived CMs, harbouring the compound *AARS2* mutations, CMs were more prone to arrhythmic events than their respective isogenic controls and the independent control.

## Lower calcium and NaV1.5 ion-channel sensitivity revealed by flecainide treatment in MEA

To further exacerbate the phenotype in Pt 1, we performed a small drug screen in hiPSC-CMs of Pt 1, Iso 1 and Ctrl, pacing at 1 Hz. In the presence of both 5 µM Thapsigargin, an inhibitor of the sarcoplasmic/endoplasmic reticulum $Ca^{2+}$ ATPase (SERCA) pump, and 15 µM flecainide, a potent anti-arrhythmic drug blocking the Ryanodine receptor 2 (RYR2), the cardiac sodium channel NaV1.5, and the human Ether-à-go-go-Related Gene (hERG), none of the hiPSC-CMs be paced at 1 Hz. The calcium transients changed to show a typical "shoulder" during the downslope of the calcium transient that is thought to be a precursor for early afterdepolarisations (EAD) (Blinova *et al.,* 2017). This was more apparent in the Ctrl and Iso 1 lines, and subsequently led to actual EAD-induced sustained triggered activity in the Ctrl line (Fig. 5A). Quantification confirmed that Pt 1 hiPSC-CMs had a weaker drug response compared to both Iso 1 and Ctrl, with the changes in beat rate, decay slope, transient area, PWD50 and PWD90 all being less pronounced (Fig. 5B).

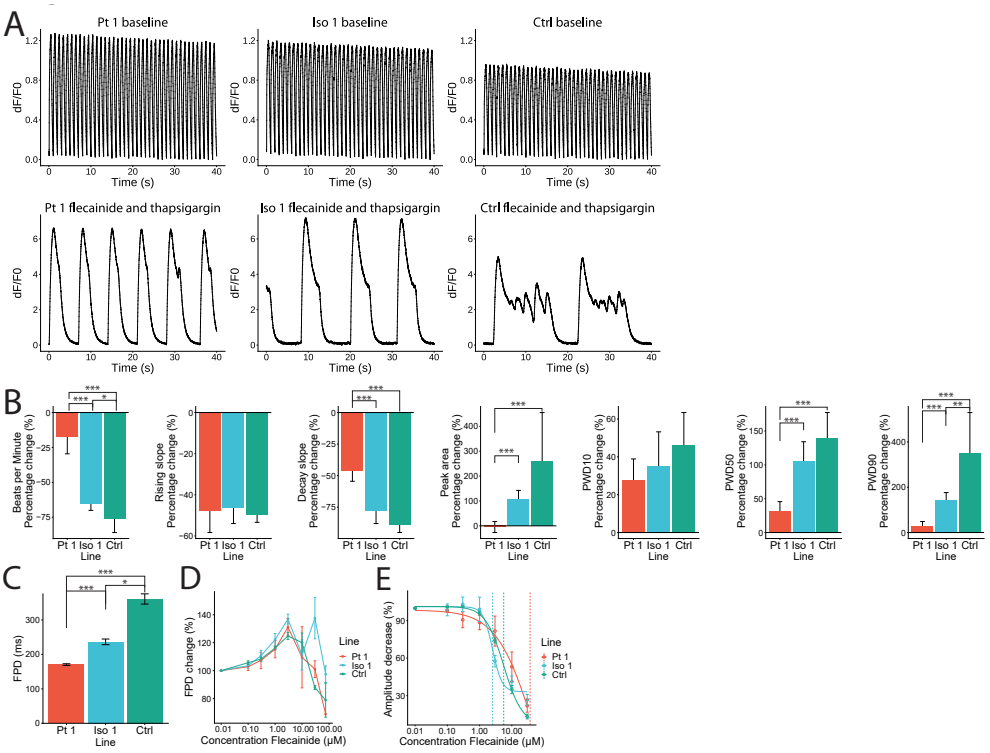


***Figure 5: Calcium, contraction and electrophysiological properties of hiPSC-CMs.***
A) Representative calcium transients from cardiomyocytes paced at 1 Hz (top) at baseline without drug intervention and at 1 Hz (bottom), including 15 μM Flecainide and 5 μM thapsigargin. B) Quantification of calcium transients parameters after the addition of flecainide and thapsigargin. DMSO treatment was used as a reference control. N = 8 and n = 2 biological repeats. Statistics indicated as follows, * P < 0.05, ** P < 0.01, *** P < 0.001 with Wilcoxon signed-rank test. C) Field potential duration (FPD) as assessed by multi-electrode array measurements. N ≥ 18, n = 2 biological repeats. Statistics indicated as follows, * P < 0.05, ** P < 0.01, *** P < 0.001 with student's t-test. D-E) FPD change (D) sodium spike amplitude change (E) upon Flecainide treatment. N ≥ 6 and n = 2 biological repeats. For amplitude decrease, the EC50 = 36.8, 2.52 and 5.59 μM for Pt 1, Iso 1 and Ctrl, respectively. All data shown are mean with standard error.

Because EADs are an arrhythmic response of cardiomyocytes to hERG-channel blockers, we investigated whether the arrhythmic behaviour we observed was due to hERG inhibition. Treatment with either thapsigargin or flecainide alone showed that the effect was solely due to flecainide (Fig. S7A), which is known to block hERG with an EC50 of 1.5 μM (Melgari *et al.,* 2014). Indeed, the transcriptomic analysis revealed that key genes related to excitation-contraction coupling had an altered expression profile in Pt 1, possibly impacting action-potential generation (Fig. S7B); however, well-known NaV1.5 modulator *SIRT1* and was not altered (Fig. S7C).

To verify whether the arrhythmic behaviour was caused by hERG blocking, we measured the hiPSC-CM field potential duration (FPD) using MEAs. Interestingly, FPDs of Pt 1 hiPSC-CMs were shorter than Iso 1 or Ctrl hiPSC-CMs (Fig. 5D). When treating the hiPSC-CMs with flecainide, the change in FPD between the lines was similar, suggesting that the hERG-blockage effect of flecainide did not drive the mechanism of action behind the observed differences in the calcium transients. (Fig. 5E). Instead, EADs observed in the calcium measurements were likely driven due to sodium-channel blockage by flecainide, where Pt 1 showed a lower sensitivity to the drug with a smaller reduction in spike amplitude (Fig. 5F).

Altogether, these results indicated a difference in ion-channel and calcium handling in Pt 1 hiPSC-CMs, resulting in altered drug response and decreased FPD *in vitro*.

# DISCUSSION

Infantile cardiomyopathy is a devastating and fatal disorder that presents shortly after birth and is often caused by mitochondrial defects. Currently, no effective treatment exists for these young patients, and it is unclear how mitochondrial defects lead to the development of cardiomyopathies.

In this study, we used previously described patient hiPSC lines (van Helden *et al.,* 2021). We generated isogenic control lines by repairing the maternally inherited mutation to investigate how the *AARS2* mutations impacted essential pathways for cardiomyocyte function.

The undifferentiated hiPSCs from the patients were not able to grow at higher confluencies, resulting in massive cell death and complete colony collapse within 24 hours. While this behaviour is not evident in the Ctrl line or any other of our regular in-house lines, it was not fixed by correcting the maternal allele. Further metabolic characterisation of the hiPSC-lines could also not explain the observed phenotype, with an increase in non-glycolytic acidification in the Ctrl-line, but these differences were not sufficient to show a lower glycolytic activity,

It is therefor tempting to speculate that the *AARS2* c.1774C>T mutation, even in heterozygosity, might result in impaired mitochondrial respiratory function since all the hiPSC lines, patients' (*AARS2*$^{c.1774C>T/c.2872C>T}$) and isogenic controls (*AARS2*$^{c.1774C>T/WT}$), showed similar behaviour. However, a mutation-cause effect could not be ruled out due to potential line-to-line and sex differences. In addition, the undifferentiated patient and isogenic hiPSC lines showed differences in the acidification rates compared to the control, possibly resulting in more rapid acidification of the medium during normal culture conditions. Only Pt 2 showed decreased OXPHOS potential compared to Iso 2 and Ctrl, while Pt 1 remained unchanged compared to Iso 1 and Ctrl. It is possible that the *AARS2* c.1774C>T mutation on the paternal allele can impair cellular function in hiPSCs. However, based

on our data, we cannot exclude the possibility of other factors playing a role, such as sex and epigenetic status of the primary samples from which the hiPSCs were derived.

The patients in this study and others diagnosed with COXPD8 showed a substantial reduction in mitochondrial complexes I, III and IV and consequent loss of COX activity in the heart (Kamps *et al.,* 2018). Here, we found reduced respiratory capacity and reduced abundance of complex IV in Pt 1 hiPSC-CMs, suggesting that our *in vitro* COXPD8 infantile cardiomyopathy hiPSC model recapitulates these important aspects of the disease. However, we did not observe complete ablation of the OXPHOS complexes I, III and IV. In an earlier study in patients diagnosed with the same pathology, a greatly reduced abundance of these OXPHOS protein complexes was described in both heart and skeletal muscle biopsies (Sommerville *et al.,* 2019). However, skin fibroblasts from these same patients remained capable of assembling these complexes, while mt-AlaRS abundance was still markedly reduced, similar to the patient hiPSC-CMs presented in this study. This illustrates the tissue specificity of mitochondrial diseases, where cells or tissues from different organs can be differently affected. The immature state of hiPSC-CMs, could explain the presence of complex I and III in our patient. Our hiPSC-CMs are more resemblant of fetal-like cardiomyocytes, while it is known that the mitochondria develop rapidly in the first weeks post-natal (Piquereau & Ventura-Clapier, 2018; Tylková, 2009; Anmann *et al.,* 2014). Indeed, most patients make it to birth, often without pre-natal signs of cardiac impairment (Euro *et al.,* 2015; Mazurova *et al.,* 2016). The metabolic switch towards predominant fatty-acid utilisation in the neo-natal heart is a major factor that drives cardiomyocyte maturation, including mitochondrial development (Ulmer & Eschenhagen, 2020; Lopaschuk & Jaswal, 2010; Piquereau & Ventura-Clapier, 2018). We speculate that these metabolic changes, along with increased mechanical load upon birth, are a deadly trigger in the heart of these young patients. Our study, based on relatively immature hiPSC-CMs that have not undergone the metabolic switch towards fatty-acid metabolism, may not reveal the entire phenotype. Nevertheless, we did find early signs of pathology, leading us to hypothesise that the patient's heart must already be predisposed to developing the disease, but that the cells have enough compensatory mechanisms in place to buffer for the loss in function.

In addition to changes in mitochondrial protein expression, the patients also showed abnormal mitochondrial morphology in the heart (Kamps *et al.,* 2018). Mitochondria are highly malleable organelles changing shape and size by fusion and fission, as well as changing their cristae ultrastructure and mitochondrial membrane potential depending on their cellular context (Vafai & Mootha, 2012). Our study found that these mitochondrial dynamics were also affected in the *AARS2* patient hiPSC-CMs. We observed an increase in both the mtDNA copy number, MMP and mean mitochondrial volume but no differences in the mitochondrial cristae ultrastructure. During fetal heart development, the absolute mtDNA copy number increases, although it remains the same

in relation to the absolute mass of the heart (Pohjoismäki *et al.,* 2013). Increases in mtDNA copy number are frequently observed during mitochondrial dysfunction and metabolic diseases, and it has been hypothesised that this is a cellular compensatory mechanism to increase mitochondrial biomass and energetic capacity (McManus *et al.,* 2019; Li *et al.,* 2018). In this regard, the increase in MMP in Pt 1 and Pt 2 was striking, as mitochondrial dysfunction is often associated with a decreased MMP. However, several other published studies have shown similar increases in the MMP in relation to mitochondrial dysfunction (McManus *et al.,* 2019; Otten *et al.,* 2018). A possible explanation is a reduction in the availability of $NAD^+$ in the patient hiPSCs-CMs. $NAD^+$ regeneration can be achieved in the mitochondria through the ETC-mediated NADH oxidation produced in the TCA cycle. Alternatively, in cells with ETC dysfunction, $NAD^+$ regeneration may also occur from pyruvate in the cytosol, through the reduction step to lactate, by lactate dehydrogenase (LDH). While intracellular pyruvate levels between all hiPSCs-CMs do not differ, we found less lactate production in the patient cells. Thus, in both the mitochondria and the cytosol, $NAD^+$ regeneration is limited in the patient hiPSCs-CMs. The role of $NAD^+$ concentration and $NAD^+$/NADH ratio has been well described in the literature in the context of cardiovascular disease, and recent investigation has solidified the relationship between reduced $NAD^+$ and metabolic, cardiac diseases, including bradycardia, to altered regulation of the NaV1.5 channel (Yoon *et al.,* 2022). Here the NADH-dependent acetylation activity of SIRT1 is the key modulator of NaV1.5, altering the excitability of the hiPSC-CMs. In our study, we observed arrhythmic behaviour, reduced NaV1.5 expression and blockage sensitivity (induced by flecainide) in our patient hiPSC-CMs, and reduced intracellular $NAD^+$ concentrations. The RNA-seq data indicated only slightly increased NAD-dependent deacetylase sirtuin 2 (*SIRT2*) expression, and *SIRT1* expression remained unchanged (Kane & Sinclair, 2018). We have not been able to uncover the exact nature of what causes the increased incidence of arrhythmia in the patient hiPSC-CMs, warranting further investigation. However, it seems likely that the combination of reduced $NAD^+$ availability and reduced expression of NaV1.5 lie at the origin.

Our metabolomics analysis also showed further evidence of altered $NAD^+$-dependent processes. Aspartate was the only amino acid increased in patient and isogenic hiPSCs-CMs, while Pt 1 also consumed significantly more aspartate from the culture medium. Aspartate *de novo* synthesis usually takes place in the mitochondria via malate dehydrogenase 2 (MDH2) and Glutamic-Oxalacetic Transaminase 2 (GOT2) and is then transported to the cytosol, where the cytosolic aspartate aminotransferase GOT1 consumes aspartate to transfer electrons into the mitochondria. However, aspartate synthesis via the $NAD^+$-dependent MDH2 is limited in cells with ETC dysfunction. This induces a shift in bidirectional GOT1 to generate aspartate in the cytosol instead of consuming it by utilising oxalacetate (Birsoy *et al.,* 2015). In agreement with this, we found an upregulation of *GOT1* in Pt 1. The necessary source of oxalacetate for GOT1 is further supported by i) the upregulation of

*DLAT* in Pt1, which catalysis the conversion of pyruvate to AcCoA in the mitochondria, which in turn can enter the TCA cycle to form citrate, ii), the upregulation of *ACLY* in Pt 1 which converts glutamine-derived citrate in the cytosol to oxalacetate and iii), the increased uptake of glutamate by the patient hiPSCs-CMs which can further contribute to the synthesis of oxaloacetate. The fact that glutamine- or glutamate- derived reductive synthesis of aspartate also requires $NAD^+$ (Sullivan *et al.,* 2015), which is limited in Pt 1 cells, might also explain the significantly higher uptake of aspartate from the culture medium by the patient hiPSCs-CMs. It is well known that increased aspartate biosynthesis or its exogenous addition rescues cell proliferation in cells with impaired ETC, regardless of which ETC-complex shows dysfunction (Birsoy *et al.,* 2015; Sullivan *et al.,* 2015). In the same studies, it was also shown that adding aspartate does not restore $NAD^+$/NADH ratio in cells with reduced respiration but rather supported proliferation via the biosynthesis of nucleotides.

Many previous studies have shown the essential role that mitochondria play in excitation-contraction coupling and calcium handling. It is, therefore, not surprising that calcium handling abnormalities have been previously identified in hiPSC-CM models for mitochondrial cardiomyopathy (Knottnerus *et al.,* 2020; Liu *et al.,* 2021; Li *et al.,* 2018; Lee *et al.,* 2016; Hallas *et al.,* 2018). Here we show that moderate changes in mitochondrial function and ATP availability are linked with disrupted calcium handling and contraction in hiPSC-CMs and, in addition, electrophysiological changes. The evident arrhythmia observed in the calcium transient measurements in our hiPSC-CMs, their inability to follow higher pacing frequencies and their altered sensitivity to flecainide illustrate the interplay between mitochondria and the calcium handling in the heart.

Patients with *AARS2* mutations frequently present with an HCM phenotype, including reduced cardiac contractile capacity and arrhythmic events. It is interesting to note that mitochondrial and calcium dysfunction underlies the decrease in heart function in HCM, like acquired HCM (caused by increased strain on the heart) or familial HCM (mainly due to mutations in sarcomeric proteins) (Lan *et al.,* 2013; Mosqueira *et al.,* 2018, 2019; Smith *et al.,* 2018; Zhou *et al.,* 2019). Mutations in myosin-binding proteins have also been shown to disrupt mitochondrial, and calcium handling in both humans and mice, and the mitochondrial disruptions are thought to be caused by an increased ATP demand by the sarcomeres, leading to increased oxidative stress (Wijnker *et al.,* 2019, 2016; McNamara *et al.,* 2017; Parbhudayal *et al.,* 2020; Güçlü *et al.,* 2017). While we do find transcriptomic evidence of HCM in our patient hiPSC-CMs, 2D hiPSC-CM models are not ideally suited to model the more severe outcomes of HCM, such as the increase in cell-size and the reduction in contractile strength. Regardless, the underlying mechanisms leading to the progressive nature of HCM are evident in our data, the early incidences of arrhythmia triggered by decreased mitochondrial function and abbarant calcium dynamics.

How increased mitochondrial stress leads to further developing calcium and contractile defects is currently not fully understood. These changes were observed in our model, which represents a fetal-like stage of cardiomyocyte development, thereby revealing early phenotype development not described before in patients with COXPD8. Our model could be used in future studies to understand how early mitochondrial dysfunction interacts with excitation-contraction coupling, uncover the cascade of events that lead to COXPD8 cardiac failure, and possibly test potential pharmacological or metabolic interventions.



In summary, we have shown that compound mutations in *AARS2* lead to insufficiencies in OXPHOS and glycolysis and can disrupt excitation-contraction coupling resulting in defective calcium homeostasis and arrhythmic behaviour in the patient hiPSC-CMs and revealing dysfunction in the entire cascade central to cardiomyocyte function. It is possible that by carefully controlling the energy source supplied to the neonate at birth, the development of life-threatening cardiomyopathy could be slowed down or even prevented.

# MATERIAL AND METHODS

## hiPSC culture and differentiation into cardiomyocytes

LUMC0024i-A, LUMC0025i-A and LUMC0026i-A hiPSC lines, previously generated as described (van Helden *et al.,* 2021) and their isogenic corrected hiPSCs were maintained on recombinant human vitronectin in E8 medium (both Thermo Fisher Scientific). The hiPSCs were passaged as small clumps twice a week using 0.5 mM Ethylenediaminetetraacetic acid (EDTA, Thermo Fisher Scientific) in phosphate-buffered saline without $Ca2^{+}/Mg^{2+}$ ($PBS^{-}$, Thermo Fisher Scientific), and plated in E8 medium with addition of Revitacell (1:200, Thermo Fisher Scientific).

The hiPSCs were differentiated into cardiomyocytes as described previously (Campostrini *et al.,* 2021), with the following modifications: on day -1, $1.5\text{-}3.5*10^4$ cells per $cm^2$ cells were plated on growth factor-reduced Matrigel-coated plates (150 µg/ml) and cardiac mesoderm was induced on day 0 using LI-BPEL medium with the concentrations of the following cytokines differing per line: Activin A (15, 30, 30 ng/ml, Pt 1/Iso 1, Pt 2/Iso 2, and Ctrl, respectively, Miltenyi Biotec), BMP4 (20, 10, 15 ng/ml, Pt 1/Iso 1, Pt 2/Iso 2, and Ctrl, respectively, R&D Systems) and CHIR99021 (1.5 µM, Axon Medchem). After 48 h, the medium was replaced with LI-BPEL containing XAV939 (5 µM, Tocris), then refreshed every 2-3 days thereafter. Enrichment for the cardiomyocyte population was performed by metabolic treatment from day 12-16 in DMEM without glucose (Thermo Fisher Scientific) with 5mM sodium L-lactate (Sigma-Aldrich). All the differentiations resulted in 85-95% of TNNT2+ cells as measured by flow cytometry (Fig. 1E, Fig. S1G). The hiPSC-CMs were dissociated

using the Multi-tissue dissociation kit 3 (Milntenyi Biotec) for 10 min at 37°C and cryopreserved in KnockOut Serum Replacement (KOSR, Thermo Fisher Scientific) with 10% DMSO (van den Brink *et al.,* 2020).

## Correction of *AARS2* c.2872C>T using CRISPR/Cas9

Genetic correction of the *AARS2* c.2872C>T mutation was performed by transfecting the hiPSCs with a gRNA recognising the mutated allele, high-fidelity Cas9 Ribonucleoprotein (RNP, IDT), and a single-stranded oligonucleotide (ssODN) comprising the corrected sequence and several silent mutations to avoid re-cutting of the Cas9 after homologous recombination. Briefly, the hiPSCs were dissociated into single cells using Accutase (Accutase) and a total of $1*10^5$ cells were electroporated using the NEON electroporation kit and the NEON Transfection system (Thermo Fisher Scientific) with 240 ng gRNA, 1 µg Cas9 RNP and 13.3 µM ssODN according to the manufacturer's recommendation. The cells were plated into a 48-well plate pre-coated with Synthemax-II substrate (6µg/ml, Corning) and containing CloneR E8 (Stemcell Technologies). After 24 h, the cells were refreshed with TesR E8 (Stemcell Technologies) and cultured until near confluence. These bulk transfected cells were dissociated with Accutase and plated at clonal density (1500 cells) in CloneR E8 on a 10 cm dish pre-coated with Synthemax-II. The remainder of the cells were used for DNA isolation, followed by ddPCR screening for identifying successful correction. The cells plated at clonal density were picked, expanded, and frozen, and DNA was isolated for a final ddPCR screen to determine which clones had successfully undergone homologous recombination. Sequences for the gRNA and ssODN can be found in Table S1.

## ddPCR for CRISPR/Cas9 correction screening and for estimating mitochondrial copy number

Genomic DNA was isolated using the high pure PCR template preparation kit (Roche) as described by the manufacturer. The ddPCR screen for identifying corrected clones was based on a double probe approach (Miyaoka *et al.,* 2014) that allowed simultaneous detection of WT, mutant and corrected alleles. The FAM probe targeting the WT allele was designed to allow binding of the mutant allele as well, while the HEX probe was designed only to bind the corrected allele (Table S1). For each sample, no more than 60 ng gDNA was mixed with both probes, ddPCR supermix for probes (Biorad) and 50 units of restriction enzymes CviQI and HindIII-HF (both from NEB), and each sample was placed in a 96-well twin-tech semi skirted PCR plate (Eppendorf). Droplet generation, PCR-amplification and droplet reading were performed using an AutoDG droplet generator, T100 Thermocycler and QX200 Droplet Digital PCR System (all from Biorad). Analysis was performed using Quantasoft™ Analysis Pro V.1.0.596 (Biorad).

Mitochondrial copy number was determined using a HEX probe targeting the nuclear *RPP30* gene and a FAM probe targeting the mitochondrially encoded *ND4* gene (BioRad). DNA was isolated from hiPSC-CMs using a chloride-based DNA lysis buffer consisting of 10 mM Tris-HCl (Merck) pH 8.0, 1 mM EDTA pH 8.0, 50 mM KCl and 2 mM MgCl2 (Sigma-Aldrich) with the addition of Proteinase K (Thermo Fisher Scientific) (200 µg/ml). The cells were lysed overnight at 60°C. The ddPCR procedure was adjusted to use 4 units of HaeIII per reaction and 2.5 ng of DNA. Due to the greater abundance of mtDNA compared to nDNA, less DNA was loaded to ensure empty droplets allowing proper quantification of DNA copies. Mitochondrial copy number estimation was calculated in R (v. 4.0.3) based on the mathematical model described previously (Dube *et al.,* 2008). Sequences of the ddPCR probes and primers can be found in Table S1.

## Mutation screening

Genomic DNA was amplified by polymerase chain reaction using primers surrounding the three *AARS2* mutations using the Platinum Taq HiFi (Invitrogen). The PCR products were purified (QIAquick PCR Purification Kit, Qiagen) and sent for Sanger sequencing. The sequences for the genotyping primers are listed in Table S1.

## Flow cytometry

Cardiac differentiation efficiency was assessed by flow cytometry analysis between days 17-21 of differentiation using cardiac troponin T (TNNT2) staining on fixed cells. Cardiomyocytes were dissociated as described above and subsequently fixed and permeabilised with Fix and Perm reagent A and B (Thermo Fisher Scientific). Cells were then stained in permeabilisation reagent B with Cardiac Troponin T-VioBlue (1:10 or 1:50, Miltenyi Biotec) for 15 min at RT and subsequently analysed in FACS buffer ($PBS^-$, with 2% FCS and 2mM EDTA) using a MACSQuant VYB flow cytometer (Miltenyi Biotec). Data were analysed using FlowJo (Tree star).

Pluripotency of the isogenic corrected hiPSC lines was assessed using the same method, using the following antibodies: OCT3/4-BV421, NANOG-PE (BD Biosciences) and SSEA-4-FITC (Miltenyi Biotec). Catalogue numbers and used dilutions for the antibodies are listed in Table S2.

## Immunocytochemistry analysis

The hiPSC-CMs were fixed in 4% paraformaldehyde, permeabilised with 0.1% Triton-X (Sigma-Aldrich) in PBS with $Ca^{2+}/Mg^{2+}$ ($PBS^+$) and blocked with 10% fetal bovine serum (Thermo Fisher Scientific). Samples were stained overnight in blocking buffer at 4°C degrees with primary antibodies

against TNNT2 (rabbit polyclonal 1:1000, Abcam) and ACTN2 (mouse monoclonal 1:800, Sigma-Aldrich). Primary antibodies were counter stained using Alexa-Fluor 488 (Goat-α-rabbit, 1:200, Thermo Fisher Scientific) and Alexa-Fluor 594 (Donkey-α-mouse 1:200, Thermo Fisher Scientific), and nuclei were stained with DAPI (Thermo Fisher Scientific). Images were acquired on a Leica SP8 WLL confocal laser-scanning microscope. Catalogue numbers and used dilutions for the antibodies are listed in Table S2.

## Western blot

The hiPSC-CMs were lysed on ice in a RIPA lysis and protein extraction buffer (Thermo Fisher Scientific) with an additional 2 µl/ml protease inhibitor mix (Sigma Aldrich). Protein content was quantified using a BCA protein kit (Thermo Fisher Scientific). 30 µg proteins per sample were used for Western blot experiments. Proteins were resolved by SDS-PAGE gel (4-15% Criterion Precast Gel, Bio-Rad) and subsequently transferred to a Polyvinylidene fluoride (PVDF) membrane (Bio-rad). Total protein was assessed by Ponceau staining before being blocked by incubation with TBS with 0.1% tween 20 with 5% non-fat dry milk for 1 h at RT. Primary antibodies against mt-AlaRS, NDUFB8, SDHA, UQCRC2, MTCO1, ATPB and VDAC1 (all Abcam) were incubated overnight at 4°C in milk on the membrane. The membrane was subsequently washed in TBS with 0.1% tween-20 and incubated with the isotype appropriate HRP-conjugated antibody (Cell Signalling) for 1 h at RT. Images were acquired with ChemiDoc MP Imaging System (Biorad) and quantified with ImageJ 1.8.0_66. Catalogue numbers and used dilutions for the antibodies are listed in Table S2.

## Transmission electron microscopy (TEM)

hiPSC-CMs were fixed for 1 h by adding to the culture medium an equal volume of fixative (3% glutaraldehyde in 0.1 M cacodylate buffer pH 7.4). After washing the monolayers three times with 0.1 M cacodylate buffer, the cells were postfixed for 1 h on ice with 1% $OsO_{4,}$ 1.5% potassium ferricyanide in 0.1M cacodylate buffer, followed by dehydration in a series of washing steps consisting of ethanol and ethanol mixed with EPON (LX112, Ladd research industries). After the final step with EPON only, BEEM capsules were filled with EPON and positioned on the fixed cells. After polymerisation of the EPON, the BEEM capsules were snapped off the surface of the culture dishes. Ultrathin sections (90 nm) parallel to the surface was made on a Reichert Ultracut S (Leica Microsystems). After the post staining of the sections with uranyl acetate and lead citrate, the electron microscopy images were taken with a twin transmission electron microscope (Thermo Fisher Scientific (formerly Fei) operating at 120 kV, using a Gatan Oneview camera (Gatan, Pleasanton) on binning 2. Overlapping images were collected and stitched together into a large image as described (Faas *et al.,* 2012).

## Live imaging of mitochondrial membrane potential and mitochondrial network

hiPSC-CMs were thawed and allowed to recover for 4 days in LI-BPEL medium. After recovery, the cells were dissociated and plated onto a glass 18-chamber slide (Ibidi) coated with 75 µg/ml Matrigel. Four days post-seeding, the hiPSC-CMs were treated and measured as previously described (Rech *et al.,* 2019). Briefly, the mitochondria were stained for 30 min with 10 nM of TMRM (Thermo Fisher) in a medium without phenol red at 37°C and 5% $CO_2$. Images were acquired using a spinning disk CorrSight fluorescent microscope equipped with a Zeiss 63x numerical aperture (NA) 1.4 objective and a Hamamatsu ORCA-Flash 4.0 V2 camera (FEI). The fluorescent signal was acquired using a 561 nm laser coupled to a 600 nm emission filter. The cells were maintained within a bioculture chamber at 37°C and 5% $CO_2$. The images consisted of 10 fields of view per well, and the z stacks contained 100 images at a Nyquist Z-distance of 170 nm. The z stacks underwent deconvolution using the Constrained Inference for Linear Mixed-Effects Models (CLME) algorithm of Huygens Professional (SVI Hilversum). Image quantification was performed using MATLAB 2017 (Mathworks) in 3D. Further data analysis was performed in R (4.0.3), and the data was normalised to the average values of the Ctrl line for each replicate.

## Measurement of oxidative and glycolytic metabolic capacity

Respiration and acidification rates of hiPSCs and hiPSC-derived cardiomyocytes were assessed using a Seahorse XF-96 Analyzer (Agilent). For undifferentiated hiPSCs, the cells were plated the day before the assay in E8 medium in an assay plate coated with vitronectin. On the day of the assay, the cells were washed and kept for 1 h in the assay medium consisting of Dulbecco's Modified Eagle Medium (DMEM) without bicarbonate (Sigma-Aldrich), 5 mM glucose (Sigma-Aldrich), 2 mM L-glutamine (Thermo Fisher Scientific), 2 mM pyruvate (Thermo Fisher Scientific) and 5 mM 4-(2-hydroxyethyl)-1-piperazineethanesulfonic acid (HEPES, Sigma-Aldrich) for performing the mitochondrial stress test and the same medium without glucose for assessing the glycolytic capacity. For assessing OXPHOS, 1 µM Oligomycin, 0.5 µM FCCP and 1 µM Antimycin A and Rotenone were injected, while for measuring glycolysis, 5 mM glucose, 1 µM Oligomycin and 10 mM 2-DG were injected (Sigma-Aldrich). Measurements of the metabolic capacity of the hiPSC-CMs were performed as follows. Thawed cardiomyocytes were plated on 75 µg/ml Matrigel in LI-BPEL four days before the assay. The medium consisted of bicarbonate DMEM, 5 mM glucose, 2 mM L-glutamine, 5 mM HEPES and 0.22% fatty acid-free BSA (Bovogen) for assessing OXPHOS and without glucose for assessing glycolytic capacity. The drug injection concentrations were adjusted to 2.5 µM Oligomycin, 2.5 µM FCCP, 2 µM Antimycin A and Rotenone, 5 mM Glucose and 100 mM 2-DG. After the assay, normalisation was performed using a Pico-green assay (Thermo Fisher Scientific). Quantification of

ATP production rates was calculated according to the Real-time ATP production kit. All analysis was performed using R (version 4.0.3).

## Metabolomics

Four days after hiPSC-CMs were thawed, the medium was replaced with HEPES-free LI-BPEL, made using Iscove's Modified Dulbecco's Medium (IMDM) without HEPES (Biowest). Additionally, the culture medium was added to an empty well serving as a background control. On days 0-3, 200 µL of the medium was taken from each well with hiPSC-CMs or the control well. Each medium sample was then mixed with 400 µL of ice cold (-20 °C) ultra-pure methanol (MeOH; Sigma-Aldrich), vortexed for 10 s and stored at -80°C until further processing. On day 3 after the last medium sample collection, the remaining medium was aspirated, each well was quickly washed with cold $PBS^+$ (Thermo Fisher Scientific) and liquid $N_2$ was added to each well in order to snap freeze the hiPSC-CMs.

Metabolite extraction from the medium was performed by centrifuging the mixed medium – MeOH samples at 18,000 $\chi$ *g* for 20 min at 0°C. The supernatant containing the metabolites in the medium was collected and dried under nitrogen gas.

Extraction of both polar and nonpolar fractions from the cells was performed as follows. Keeping the plate on ice, 600 µL of 0°C 60% (v/v) MeOH was added to each well, and cells were lysed using a scraper. The lysate was transferred to pre-cooled Eppendorf tubes and vortexed for 10 min at 4°C. Subsequently, 500 µL of 0°C chloroform (Sigma-Aldrich) was added, and the tubes were vortexed for an additional 10 min at 4°C and then left at -40°C for 30 min to allow separation of the polar and nonpolar phases. Samples were then centrifuged at 4,000 $\chi$ *g* for 10 min at 4°C. The polar (upper) and nonpolar (bottom) phases were collected and transferred to glass vials. All extracts were dried under nitrogen gas and stored at -80°C until further processing. The middle protein-containing layer form each sample was dissolved in a buffer consisting of 3M Urea (Sigma-Aldrich), 0.25M TRIS-HCl (Merck) at pH 8.0 and 1% SDS (Sigma-Aldrich) and was subsequently quantified by Pierce BCA protein assay (Thermo Fisher Scientific) for normalisation of the metabolomics data.

Polar cell extracts and media extracts were dissolved in 0.22mL 50mM $K_2HPO_4/KH_2PO_4$ (Sigma-Aldrich) solution (pH 7.4) in 99.9% deuterated water ($D_2O$; CortecNet) containing 0.2 mM $NaN_3$ (Sigma-Aldrich) and 0.05 mM of trimethylsilylpropionic-$d_4$ acid sodium salt (TSP-d4; Sigma-Aldrich). From each sample, 185 µL were transferred to 3 mm Nuclear Magentic Resonance (NMR) tubes (Bruker), and quantitative metabolomics was performed by NMR spectroscopy as described in detail previously (Kostidis *et al.,* 2017). Briefly, NMR spectra were recorded using a 14.1T NMR spectrometer (600MHz for $^1H$; Bruker Avance Neo) under standardised instrumental settings for all

samples. For each sample, a one-dimensional $^{1}H$ spectrum was collected using the *noesygppr1d* pulse sequence. All spectra data were phased, baseline corrected and referenced to TSP-d4 methyl protons at $\delta$ 0.00 ppm and subsequently imported into Chenomx NMR suit 8.5 (Chenomx Edmonton, Canada) for the quantification of metabolites.

Dried nonpolar cell extracts were used for lipidomic analysis by the commercial Lipidyzer platform (The Lipidyzer, Sciex). Lipid extracts were dissolved in a 250 µL buffer solution of 10 mM ammonium acetate in 50:50 (*v*/*v*) dichloromethane/methanol (Lipidyzer running buffer), including the Lipidyzer internal standard kit with >50 labelled internal standards for 13 lipid classes. The Lipidyzer platform is a flow-injection-based ion-mobility triple quadrupole system consisting of a Sciex 5500 QTrap equipped with SelexIon technology coupled to a Shimadzu Nexera series UHPLC system used for injection and delivering running buffer at 7 µL/min. A total of 50 µL of the resuspended samples were injected using 2 dedicated methods. Method #1 operated with active differential mobility spectrometry (DMS) separation under the following conditions: DMS temperature low, modifier (propanol) composition low, separation voltage 3500 V, and DMS resolution enhancement low. For method #2, the DMS cell was not activated. The MS operated under the following conditions: curtain gas 17, CAD gas medium, ion spray voltage 4100 V in ESI + mode and −2500 V in ESI− mode, temperature 200 °C, nebulising gas 17, and heater gas 25. First, phosphatidyl choline (PC), phosphatidylethanolamine (PE), lysophosphatidyl choline (LPC), lysophosphatidylethanolamine (LPE), and sphingomyelin (SM) lipid classes were analysed with method #1. Next, free fatty acid (FFA), triacylglyceride (TAG), diacylglyceride (DAG), ceramide (CER), dihydroceramide (DCER), lactosylceramide (LCER), hexosylceramide (HCER), and cholesterol ester (CE) lipids were analysed applying method #2. Further technical detail, including a list of all monitored transitions and detailed experimental settings can be found elsewhere. All concentrations from polar metabolites and lipids (µmol /L) were normalised to the protein mass of each cell extract.

## RNA-sequencing analysis

RNA was isolated and purified from the hiPSC-CMs using the NucleoSpin RNA-kit (Macherey-Nagel). RNA-sequencing and whole-genome transcriptome data were generated by Novogene (United Kingdom) on the Illumina NovaSeq6000 platform, paired-end sequencing and read length of 150bp with a sequencing depth of 20M raw reads per sample.

Raw RNA-seq reads were processed using the open-source BIOWDL RNAseq pipeline v3.0.0 (https://zenodo.org/record/3713261#.YoQ9mxxBxhE) developed at the LUMC. This pipeline performs FASTQ preprocessing (including quality control, quality trimming, and adapter clipping), RNA-Seq alignment, read quantification, and optionally transcript assembly. FastQC was used for

checking raw read QC. Adapter clipping was performed using Cutadapt (v2.4) with default settings. RNA-Seq reads' alignment was performed using STAR (v2.7.3a) on GRCh38 human reference genome. The gene read quantification was performed using HTSeq-count (v0.11.2) with the setting "–stranded=no". The gene annotation used for quantification was Ensembl version 99.

Count tables were normalised against gene length and GC content using the R-package *cqn* v1.4 (Hansen *et al.,* 2012), and genes were filtered based on their expression across all the samples according to (Chen *et al.,* 2016), resulting in a final dataset of 19120 genes and 15 samples. Differentially expressed genes (DEG) were identified using a general linearised model based on the package EdgeR (McCarthy *et al.,* 2012), correcting for cellular origin. Benjamini and Hochberg FDR were computed to adjust p-values obtained for each differentially expressed gene. Using a cutoff of 0.05 at the adjusted p-values, we identified all up and down-regulated genes. Heatmaps were produced using the pheatmap package (Kolde, 2019). KEGG-pathway enrichment was performed based on the sum of rank test, with adjusted p-values < 0.05 considered to be significant according to the Benjamini-Hochberg procedure (Irizarry *et al.,* 2009), gene-ontology (GO) enrichment, using the Kolmogorov-Smirnov Goodness of Fit Test with a cutoff p-value of < 0.05, were performed using the topGO package (2.44 (Alexa & Rahnenfuhrer, 2021)), and mitochondrial pathway analysis enrichment was performed using the sum of rank tests, a less stringent use of un-adjusted p-values of < 0.05 considered significant. Both the tested genes and the involvement in mitochondrial processes was based on the curated MitoCarta 3.0 dataset (Rath *et al.,* 2021).

## $NAD^+$ measurements

Intracellular $NAD^+$ concentrations were Dissociated hiPSC-CMs were plated on a µclear white transparent 384 well plate (Greiner) precoated with 75 µg/ml Matrigel (Corning). After a four-day recovery period, the cells were lysed using the NAD/NADH-Glo assay (Promega) according to manufacturer's protocol, and total $NAD^+$ was measured on a SpectraMax iD3 plate reader. Data was analysed using R (4.1.1), and the data were normalised to the average values of the Ctrl line for each replicate.

## Calcium transient measurements

Calcium transients were assessed on hiPSC-CMs thawed and seeded in a black, flat-bottomed 96-well plate coated with 75 µg/ml Matrigel (Corning) and cultured for four days before the assay. The calcium-6 dye (Molecular Devices) was dissolved in 10 mL HBSS buffer B and subsequently diluted 3-fold in Buffer B (Molecular Devices). The diluted dye solution was added 1:1 to the wells containing hiPSC-CMs in a bicarbonate-free medium consisting of DMEM, 5 mM Glucose, 2 mM

L-glutamine, 1 mM pyruvate, 5 mM HEPES and 0.2% BSA. Cardiomyocytes were incubated for 1 hr at 37°C and 0% $CO_2$ before being measured on the FDSS/µcell (Hamamatsu Photonics) at 37°C and 0% $CO_2$ with an exposure time of 0.017s. Caffeine injection was performed by preparing a "compound plate" including 100 µM caffeine (Sigma Aldrich) in the assay medium, which was then automatically injected into the assay plate, reaching a final concentration of 25 µM (Liu *et al.,* 2007). Analysis was performed using R (4.0.3). Poincaré graphs were generated by plotting the peak-to-peak (PtP) interval of one cycle against the PtP-interval of the previous cycle ($PtP_{n-1}$). Ellipse statistics were calculated by taking the SD-length (deviation along the intersecting line) and SD-width (deviation perpendicular to the intersecting line), according to (Tulppo *et al.,* 1996; Fishman *et al.,* 2012) and using additional R package ggforce (Pedersen, 2021).



The pacing was performed using the EFS pacing head add-on (Hamamatsu Photonics). Cells were paced at frequencies of 0.5 or 1 Hz, with a pulse of 7.5 V, 10 ms width and the probe at the height of 0.5-1 mm. The addition of flecainide and thapsigargin was performed manually by adding a 10x concentrated stock of 150 µM and 50 µM for each, respectively. Analysis was performed in R (4.0.3), and induced change was calculated against baseline and corrected for DMSO controls.

## Contraction measurements

Thawed hiPSC-CMs were seeded in a black, flat-bottomed 96-well plate coated with 75 µg/ml Matrigel (Corning) and cultured for four days to recover. Videos of cardiomyocyte contraction were recorded on a microscope using a 40x objective (Leica Inverted microscope IBDE) with a Thorlabs DCC3240M camera at 100 frames per second. The cells were kept in a culture chamber at 37°C and 5% $CO_2$. When capturing spontaneous contraction, videos were recorded for 15-30 seconds. The pacing of the cardiomyocytes was performed with a pulse of 21V/cm for 12.5 ms. The duration of each recording was adjusted to allow for at least 4 contractions to be captured. Videos were analysed using MUSCLEMOTION (Sala *et al.,* 2018) ImageJ macro (ImageJ 1.8.0_66), and analysis was performed using R (4.0.3).

## Field potential measurements

Seven days after recovery from thaw, hiPSC-CMs were dissociated and plated onto a Matrigel-coated 48-well multi-electrode array (MEA) plate (Axion Biosystems), by adding 8 µl droplets of cell suspension containing 70k hiPSC-CMs to the middle of each well, taking care to cover the measuring electrodes and not the reference electrode. After initial attachment for 2 h in the incubator, an additional 300 µl of LI-BPEL was gently added to the wells. The cells were allowed to recover for 7 days before evaluating drug responses using the Maestro Pro MEA system (Axion Biosystems). E4031

(Torcis) and flecainide (Torcis) were dissolved in DMSO at stock concentrations of 50mM. From this stock, further dilutions were made in LI-BPEL medium with a final DMSO concentration of 0.1%. Data were analysed using R (4.0.3), and dose-response curve statistics were calculated using (Ritz *et al.,* 2015).

### Data and statistical analysis

All data analysis was performed using R (4.0.3), relying on additional packages (Wickham *et al.,* 2019; Wilke, 2020; Xie, 2021; Xiao, 2018). Data is represented as mean with standard error, and statistical analysis was performed using student's t-test or Mann-Whitney U test. P-values $< 0.05$ were considered statistically significant.

## ACKNOWLEDGEMENTS

This work was funded by the following grants: the Netherlands Organ-on-Chip Initiative, an NWO Gravitation project (024.003.001) funded by the Ministry of Education, Culture and Science of the government of the Netherlands; European Research Council (ERC-CoG 101001746 Mini-HEART; ERCAdG 323182 STEMCARDIOVASC); The Novo Nordisk Foundation Center for Stem Cell Medicine is supported by Novo Nordisk Foundation grants (NNF21CC0073729)I. MG was partially funded by NWO XOmics project #184.034.019. RdC is supported by the NeMo foundation. We want to thank: B. Everts and A.J. van der Ham (Leiden University Medical Center, LUMC) for access to the Agilent Seahorse XFe96 analyser; K.O. Brandão (LUMC) for sharing electroporation protocols to correct the AARS2 mutation in the patient lines; V.V. Orlova and F.E. van den Hill (LUMC) for assisting in the preparation of samples for transcriptomics; T.M.J. Ward-van Oostwaard (LUMC) for technical assistance; F.H.J. van Tienen (Maastricht University) for support with mitochondrial imaging; Y. Ge (LUMC) for help on the Western blots; R.J. Nell, M. Versluis-Lops and P.A. van der Velden (LUMC) for technical and statistical assistance with the ddPCR experiments; C.R. Jost and A.J. Koster (LUMC) for assistance with the TEM. The graphical abstract and the graphics in Fig. 1 D were created using https://BioRender.com.

## COMPETING INTERESTS

C.L.M. is co-founder of Ncardia bv. The authors have no additional financial interests.

## AUTHOR CONTRIBUTIONS

Conceptualisation: R.W.J.v.H, C.L.M., M.B. Formal Analysis: R.W.J.v.H, T.K., S.K., H.M., R.C.S., K.K.,

Funding Aquisition: C.L.M, M.B, M.G., R.P.D. Investigation: R.W.J.v.H, T.K., S.K., K.K., A.A.M.

Methodology: R.W.J.v.H, T.K., S.K., Project administration: R.W.J.v.H, C.L.M., M.B. Resources: R.d.C

Software: R.C.S., H.M. Supervision: M.B, C.L.M., M.M. Visualisation: R.W.J.v.H. Writing – original

draft: R.W.J.v.H, C.L.M., M.B. Writing - review & editing: R.W.J.v.H, T.K., S.K., C.L.M., M.B.

## DATA AVAILABILITY

The datasets and computer code produced in this study are available in the following databases:

- **RNA-Seq data: Gene Expression Omnibus GSE46843 (https://www.ncbi.nlm.nih.gov/geo/query/acc.cgi?acc=GSE208272)**
- Datasets of intracellular lipidomics and metabolomics as well as metabolomic measurements on medium are attached as supplemental Tables 3, 4 and 5. Data are represented as nmol normalised to the total amount (μg) of protein

# REFERENCES


Aibara S, Singh V, Modelska A & Amunts A (2020) Structural basis of mitochondrial translation. *eLife* 9: e58362

Alexa A & Rahnenfuhrer J (2021) topGO: Enrichment Analysis for Gene Ontology.

Anderson S, Bankier AT, Barrell BG, de Bruijn MH, Coulson AR, Drouin J, Eperon IC, Nierlich DP, Roe BA, Sanger F, *et al* (1981) Sequence and organization of the human mitochondrial genome. *Nature* 290: 457–465

Anmann T, Varikmaa M, Timohhina N, Tepp K, Shevchuk I, Chekulayev V, Saks V & Kaambre T (2014) Formation of highly organized intracellular structure and energy metabolism in cardiac muscle cells during postnatal development of rat heart. *Biochim Biophys Acta BBA - Bioenerg* 1837: 1350–1361

Birsoy K, Wang T, Chen WW, Freinkman E, Abu-Remaileh M & Sabatini DM (2015) An Essential Role of the Mitochondrial Electron Transport Chain in Cell Proliferation Is to Enable Aspartate Synthesis. *Cell* 162: 540–551

Blinova K, Stohlman J, Vicente J, Chan D, Johannesen L, Hortigon-Vinagre MP, Zamora V, Smith G, Crumb WJ, Pang L, *et al* (2017) Comprehensive Translational Assessment of Human-Induced Pluripotent Stem Cell Derived Cardiomyocytes for Evaluating Drug-Induced Arrhythmias. *Toxicol Sci Off J Soc Toxicol* 155: 234–247

van den Brink L, Brandão KO, Yiangou L, Mol MPH, Grandela C, Mummery CL, Verkerk AO & Davis RP (2020) Cryopreservation of human pluripotent stem cell-derived cardiomyocytes is not detrimental to their molecular and functional properties. *Stem Cell Res* 43: 101698

Campostrini G, Meraviglia V, Giacomelli E, van Helden RWJ, Yiangou L, Davis RP, Bellin M, Orlova VV & Mummery CL (2021) Generation, functional analysis and applications of isogenic three-dimensional self-aggregating cardiac microtissues from human pluripotent stem cells. *Nat Protoc* 16: 2213–2256

Chen Y, Lun ATL & Smyth GK (2016) From reads to genes to pathways: differential expression analysis of RNA-Seq experiments using Rsubread and the edgeR quasi-likelihood pipeline. doi:10.12688/f1000research.8987.2 [PREPRINT]

Chowdhury A, Aich A, Jain G, Wozny K, Lüchtenborg C, Hartmann M, Bernhard O, Balleiniger M, Alfar EA, Zieseniss A, *et al* (2018) Defective Mitochondrial Cardiolipin Remodeling Dampens HIF-1α Expression in Hypoxia. *Cell Rep* 25: 561-570.e6

Dallabona C, Diodato D, Kevelam SH, Haack TB, Wong LJ, Salomons GS, Baruffini E, Melchionda L, Mariotti C, Strom TM, *et al* (2014) Novel (ovario) leukodystrophy related to AARS2 mutations. *Neurology* 82: 2063–2071

Dube S, Qin J & Ramakrishnan R (2008) Mathematical Analysis of Copy Number Variation in a DNA Sample Using Digital PCR on a Nanofluidic Device. *PLOS ONE* 3: e2876

Dudek J, Cheng I-F, Chowdhury A, Wozny K, Balleininger M, Reinhold R, Grunau S, Callegari S, Toischer K, Wanders RJ, *et al* (2016) Cardiac-specific succinate dehydrogenase deficiency in Barth syndrome. *EMBO Mol Med* 8: 139–54

Euro L, Konovalova S, Asin-Cayuela J, Tulinius M, Griffin H, Horvath R, Taylor RW, Chinnery PF, Schara U, Thorburn DR, *et al* (2015) Structural modeling of tissue-specific mitochondrial alanyl-tRNA synthetase (AARS2) defects predicts differential effects on aminoacylation. *Front Genet* 5: 1–12

Faas FGA, Avramut MC, van den Berg BM, Mommaas AM, Koster AJ & Ravelli RBG (2012) Virtual nanoscopy: generation of ultra-large high resolution electron microscopy maps. *J Cell Biol* 198: 457–469

Fatica EM, DeLeonibus GA, House A, Kodger JV, Pearce RW, Shah RR, Levi L & Sandlers Y (2019) Barth Syndrome: Exploring Cardiac Metabolism with Induced Pluripotent Stem Cell-Derived Cardiomyocytes. *Metabolites* 9: E306

Finsterer J & Kothari S (2014) Cardiac manifestations of primary mitochondrial disorders. *Int J Cardiol* 177: 754–763

Fishman M, Jacono FJ, Park S, Jamasebi R, Thungtong A, Loparo KA & Dick TE (2012) A method for analyzing temporal patterns of variability of a time series from Poincaré plots. *J Appl Physiol* 113: 297–306

Gorman GS, Chinnery PF, DiMauro S, Hirano M, Koga Y, McFarland R, Suomalainen A, Thorburn DR, Zeviani M & Turnbull DM (2016) Mitochondrial diseases. *Nat Rev Dis Primer* 2: 16080

Götz A, Tyynismaa H, Euro L, Ellonen P, Hyötyläinen T, Ojala T, Hämäläinen RH, Tommiska J, Raivio T, Oresic M, *et al* (2011) Exome sequencing identifies mitochondrial alanyl-tRNA synthetase mutations in infantile mitochondrial cardiomyopathy. *Am J Hum Genet* 88: 635–642

Güçlü A, Knaapen P, Harms HJ, Parbhudayal RY, Michels M, Lammertsma AA, van Rossum AC, Germans T & van der Velden J (2017) Disease Stage Dependent Changes in Cardiac Contractile Performance and Oxygen Utilization Underlie Reduced Myocardial Efficiency in Human Inherited Hypertrophic Cardiomyopathy. *Circ Cardiovasc Imaging* 10: e005604

Guo M, Chong YE, Shapiro R, Beebe K, Yang X-L & Schimmel P (2009) Paradox of mistranslation of serine for alanine caused by AlaRS recognition dilemma. *Nature* 462: 808–812

Hallas T, Eisen B, Shemer Y, Ben Jehuda R, Mekies LN, Naor S, Schick R, Eliyahu S, Reiter I, Vlodavsky E, *et al* (2018) Investigating the cardiac pathology of SCO2-mediated hypertrophic cardiomyopathy using patients induced pluripotent stem cell–derived cardiomyocytes. *J Cell Mol Med* 22: 913–925

Hansen KD, Irizarry RA & WU Z (2012) Removing technical variability in RNA-seq data using conditional quantile normalization. *Biostat Oxf Engl* 13: 204–216

van Helden RWJ, Birket MJ, Freund C, Arendzen CH, Mikkers HM, Orlova V, de Coo RI, Mummery CL & Bellin M (2021) Generation of three human induced pluripotent stem cell lines, LUMCi024-A, LUMCi025-A, and LUMCi026-A, from two patients with combined oxidative phosphorylation deficiency 8 and a related control. *Stem Cell Res* 53: 102374

Hick A, Wattenhofer-Donzé M, Chintawar S, Tropel P, Simard JP, Vaucamps N, Gall D, Lambot L, André C, Reutenauer L, *et al* (2013) Neurons and cardiomyocytes derived from induced pluripotent stem cells as a model for mitochondrial defects in Friedreich's ataxia. *Dis Model Mech* 6: 608–621

Hilander T, Zhou X-L, Konovalova S, Zhang F-P, Euro L, Chilov D, Poutanen M, Chihade J, Wang E-D & Tyynismaa H (2018) Editing activity for eliminating mischarged tRNAs is essential in mammalian mitochondria. *Nucleic Acids Res* 46: 849–860

Irizarry RA, Wang C, Zhou Y & Speed TP (2009) Gene set enrichment analysis made simple. *Stat Methods Med Res* 18: 565–575

Jin H, Hilaire CS, Huang Y, Yang D, Dmitrieva NI, Negro A, Schwartzbeck R, Liu Y, Yu Z, Walts A, *et al* (2016) Increased activity of TNAP compensates for reduced adenosine production and promotes ectopic calcification in the genetic disease ACDC. 121

Kamps R, Szklarczyk R, Theunissen TE, Hellebrekers DMEI, Sallevelt SCEH, Boesten IB, Koning B de, Bosch BJ van den, Salomons GS, Simas-Mendes M, *et al* (2018) Genetic defects in mtDNA-encoded protein translation cause pediatric, mitochondrial cardiomyopathy with early-onset brain disease. *Eur J Hum Genet* 26: 537

Kane AE & Sinclair DA (2018) Sirtuins and NAD+ in the Development and Treatment of Metabolic and Cardiovascular Diseases. *Circ Res* 123: 868–885

Knottnerus SJG, Mengarelli I, Wüst RCI, Baartscheer A, Bleeker JC, Coronel R, Ferdinandusse S, Guan K, IJlst L, Li W, *et al* (2020) Electrophysiological Abnormalities in VLCAD Deficient hiPSC-Cardiomyocytes Can Be Improved by Lowering Accumulation of Fatty Acid Oxidation Intermediates. *Int J Mol Sci* 21: E2589

Kolde R (2019) pheatmap: Pretty Heatmaps.

Koopman WJH, Willems PHGM & Smeitink JAM (2012) Monogenic Mitochondrial Disorders. *N Engl J Med* 366: 1132–1141

Kostidis S, Addie RD, Morreau H, Mayboroda OA & Giera M (2017) Quantitative NMR analysis of intra- and extracellular metabolism of mammalian cells: A tutorial. *Anal Chim Acta* 980: 1–24

Lan F, Lee AS, Liang P, Sanchez-Freire V, Nguyen PK, Wang L, Han L, Yen M, Wang Y, Sun N, *et al* (2013) Abnormal calcium handling properties underlie familial hypertrophic cardiomyopathy pathology in patient-specific induced pluripotent stem cells. *Cell Stem Cell* 12: 101–13

Lee Y-K, Lau Y-M, Ng K-M, Lai W-H, Ho S-L, Tse H-F, Siu C-W & Ho PW-L (2016) Efficient attenuation of Friedreich's ataxia (FRDA) cardiomyopathy by modulation of iron homeostasis-human induced pluripotent stem cell (hiPSC) as a drug screening platform for FRDA. *Int J Cardiol* 203: 964–971

Li J, Rozwadowska N, Clark A, Fil D, Napierala JS & Napierala M (2019) Excision of the expanded GAA repeats corrects cardiomyopathy phenotypes of iPSC-derived Friedreich's ataxia cardiomyocytes. *Stem Cell Res* 40: 101529

Li S, Pan H, Tan C, Sun Y, Song Y, Zhang X, Yang W, Wang X, Li D, Dai Y, *et al* (2018) Mitochondrial Dysfunctions Contribute to Hypertrophic Cardiomyopathy in Patient iPSC-Derived Cardiomyocytes with MT-RNR2 Mutation. *Stem Cell Rep* 10: 808–821

Liu J, Fu JD, Siu CW & Li RA (2007) Functional Sarcoplasmic Reticulum for Calcium Handling of Human Embryonic Stem Cell-Derived Cardiomyocytes: Insights for Driven Maturation. *STEM CELLS* 25: 3038–3044

Liu X, Wang S, Guo X, Li Y, Ogurlu R, Lu F, Prondzynski M, de la Serna Buzon S, Ma Q, Zhang D, *et al* (2021) Increased Reactive Oxygen Species–Mediated Ca2+/Calmodulin-Dependent Protein Kinase II Activation Contributes to Calcium Handling Abnormalities and Impaired Contraction in Barth Syndrome. *Circulation* 143: 1894–1911

Lopaschuk GD & Jaswal JS (2010) Energy metabolic phenotype of the cardiomyocyte during development, differentiation, and postnatal maturation. *J Cardiovasc Pharmacol* 56: 130–40

Mazurova S, Magner M, Kucerova-Vidrova V, Vondrackova A, Stranecky V, Pristoupilova A, Zamecnik J, Hansikova H, Zeman J, Tesarova M, *et al* (2016) Thymidine kinase 2 and alanyl-tRNA synthetase 2 deficiencies cause lethal mitochondrial cardiomyopathy: case reports and review of the literature. *Cardiol Young*: 1–9

McCarthy DJ, Chen Y & Smyth GK (2012) Differential expression analysis of multifactor RNA-Seq experiments with respect to biological variation. *Nucleic Acids Res* 40: 4288–4297

McManus MJ, Picard M, Chen H-W, De Haas HJ, Potluri P, Leipzig J, Towheed A, Angelin A, Sengupta P, Morrow RM, *et al* (2019) Mitochondrial DNA Variation Dictates Expressivity and Progression of Nuclear DNA Mutations Causing Cardiomyopathy. *Cell Metab* 29: 78-90.e5

McNamara JW, Li A, Lal S, Bos JM, Harris SP, Velden J van der, Ackerman MJ, Cooke R & Remedios CG dos (2017) MYBPC3 mutations are associated with a reduced super-relaxed state in patients with hypertrophic cardiomyopathy. *PLOS ONE* 12: e0180064

Melgari D, Harchi AE, Dempsey CE & Hancox JC (2014) Sensitivity of Flecainide Inhibition of hERG Channels to Channel Inactivation. *Biophys J* 106: 138a

Miyaoka Y, Chan AH, Judge LM, Yoo J, Huang M, Nguyen TD, Lizarraga PP, So P-L & Conklin BR (2014) Isolation of single-base genome-edited human iPS cells without antibiotic selection. *Nat Methods* 11: 291–293

Mosqueira D, Mannhardt I, Bhagwan JR, Lis-Slimak K, Katili P, Scott E, Hassan M, Prondzynski M, Harmer SC, Tinker A, *et al* (2018) CRISPR/Cas9 editing in human pluripotent stem cell-cardiomyocytes highlights arrhythmias, hypocontractility, and energy depletion as potential therapeutic targets for hypertrophic cardiomyopathy. *Eur Heart J*: 1–16

Mosqueira D, Smith JGW, Bhagwan JR & Denning C (2019) Modeling Hypertrophic Cardiomyopathy: Mechanistic Insights and Pharmacological Intervention. *Trends Mol Med* 25: 775–790

Nguyen T, Alzahrani T, Krepp J & Panjrath G (2021) Cardiovascular Outcomes in Patients With Mitochondrial Disease in the United States: A Propensity Score Analysis. *Tex Heart Inst J* 48

Nielsen SK, Hansen F, Schrøder HD, Wibrand F, Gustafsson F & Mogensen J (2020) Recessive Inheritance of a Rare Variant in the Nuclear Mitochondrial Gene for AARS2 in Late-Onset Dilated Cardiomyopathy. *Circ Genomic Precis Med* 13: 560–562

Otten ABC, Sallevelt SCEH, Carling PJ, Dreesen JCFM, Drüsedau M, Spierts S, Paulussen ADC, de Die-Smulders CEM, Herbert M, Chinnery PF, *et al* (2018) Mutation-specific effects in germline transmission of pathogenic mtDNA variants. *Hum Reprod* 33: 1331–1341

Parbhudayal RY, Harms HJ, Michels M, van Rossum AC, Germans T & van der Velden J (2020) Increased Myocardial Oxygen Consumption Precedes Contractile Dysfunction in Hypertrophic Cardiomyopathy Caused by Pathogenic TNNT2 Gene Variants. *J Am Heart Assoc* 9: e015316

Pavez-Giani MG & Cyganek L (2022) Recent Advances in Modeling Mitochondrial Cardiomyopathy Using Human Induced Pluripotent Stem Cells. *Front Cell Dev Biol* 9

Pedersen T Lin (2021) ggforce: Accelerating 'ggplot2'.

Piquereau J & Ventura-Clapier R (2018) Maturation of Cardiac Energy Metabolism During Perinatal Development. *Front Physiol* 9

Pohjoismäki JLO, Krüger M, Al-Furoukh N, Lagerstedt A, Karhunen PJ & Braun T (2013) Postnatal cardiomyocyte growth and mitochondrial reorganization cause multiple changes in the proteome of human cardiomyocytes. *Mol Biosyst* 9: 1210–1219

Rath S, Sharma R, Gupta R, Ast T, Chan C, Durham TJ, Goodman RP, Grabarek Z, Haas ME, Hung WHW, *et al* (2021) MitoCarta3.0: an updated mitochondrial proteome now with sub-organelle localization and pathway annotations. *Nucleic Acids Res* 49: D1541–D1547

Rech M, Kuhn AR, Lumens J, Carai P, van Leeuwen R, Verhesen W, Verjans R, Lecomte J, Liu Y, Luiken JJFP, *et al* (2019) AntagomiR-103 and -107 Treatment Affects Cardiac Function and Metabolism. *Mol Ther - Nucleic Acids* 14: 424–437

Ritz C, Baty F, Streibig JC & Gerhard D (2015) Dose-Response Analysis Using R. *PLOS ONE* 10: e0146021

Rohani L, Machiraju P, Sabouny R, Meng G, Liu S, Zhao T, Iqbal F, Wang X, Ravandi A, Wu JC, *et al* (2020) Reversible Mitochondrial Fragmentation in iPSC-Derived Cardiomyocytes From Children With DCMA, a Mitochondrial Cardiomyopathy. *Can J Cardiol* 36: 554–563

Sala L, van Meer BJ, Tertoolen LGJ, Bakkers J, Bellin M, Davis RP, Denning C, Dieben MAE, Eschenhagen T, Giacomelli E, *et al* (2018) Musclemotion. *Circ Res* 122: e5–e16

Smith JGW, Owen T, Bhagwan JR, Mosqueira D, Scott E, Mannhardt I, Patel A, Barriales-Villa R, Monserrat L, Hansen A, *et al* (2018) Isogenic Pairs of hiPSC-CMs with Hypertrophic Cardiomyopathy/LVNC-Associated ACTC1 E99K Mutation Unveil Differential Functional Deficits. *Stem Cell Rep* 11: 1226–1243

Sokabe M, Ose T, Nakamura A, Tokunaga K, Nureki O, Yao M & Tanaka I (2009) The structure of alanyl-tRNA synthetase with editing domain. *Proc Natl Acad Sci U S A* 106: 11028–11033

Sommerville EW, Zhou X-L, Oláhová M, Jenkins J, Euro L, Konovalova S, Hilander T, Pyle A, He L, Habeebu S, *et al* (2019) Instability of the mitochondrial alanyl-tRNA synthetase underlies fatal infantile-onset cardiomyopathy. *Hum Mol Genet* 28: 258–268

Sullivan LB, Gui DY, Hosios AM, Bush LN, Freinkman E & Vander Heiden MG (2015) Supporting Aspartate Biosynthesis Is an Essential Function of Respiration in Proliferating Cells. *Cell* 162: 552–563

Tang Y, Qin Q, Xing Y, Guo D, Di L & Jia J (2019) AARS2 leukoencephalopathy: A new variant of mitochondrial encephalomyopathy. *Mol Genet Genomic Med* 7: e00582

Taylor RW, Pyle A, Griffin H, Blakely EL, Duff J, He L, Smertenko T, Alston CL, Neeve VC, Best A, *et al* (2014) Use of Whole-Exome Sequencing to Determine the Genetic Basis of Multiple Mitochondrial Respiratory Chain Complex Deficiencies. *JAMA* 312: 68

Tulppo MP, Mäkikallio TH, Takala TE, Seppänen T & Huikuri HV (1996) Quantitative beat-to-beat analysis of heart rate dynamics during exercise. *Am J Physiol* 271: H244-252

Tylková L (2009) Architectural and functional remodeling of cardiac and skeletal muscle cells in mice lacking specific isoenzymes of creatine kinase. *Gen Physiol Biophys* 28: 219–224

Ulmer BM & Eschenhagen T (2020) Human pluripotent stem cell-derived cardiomyocytes for studying energy metabolism. *Biochim Biophys Acta BBA - Mol Cell Res* 1867: 118471

Vafai SB & Mootha VK (2012) Mitochondrial disorders as windows into an ancient organelle. *Nature* 491: 374–383

Wang G, McCain ML, Yang L, He A, Pasqualini FS, Agarwal A, Yuan H, Jiang D, Zhang D, Zangi L, *et al* (2014) Modeling the mitochondrial cardiomyopathy of Barth syndrome with induced pluripotent stem cell and heart-on-chip technologies. *Nat Med* 20: 616–623

Watanabe K (2010) Unique features of animal mitochondrial translation systems. The non-universal genetic code, unusual features of the translational apparatus and their relevance to human mitochondrial diseases. *Proc Jpn Acad Ser B Phys Biol Sci* 86: 11–39

Wickham H, Averick M, Bryan J, Chang W, McGowan LD, François R, Grolemund G, Hayes A, Henry L, Hester J, *et al* (2019) Welcome to the Tidyverse. *J Open Source Softw* 4: 1686

Wijnker PJM, Friedrich FW, Dutsch A, Reischmann S, Eder A, Mannhardt I, Mearini G, Eschenhagen T, Velden J van der & Carrier L (2016) Comparison of the effects of a truncating and a missense MYBPC3 mutation on contractile parameters of engineered heart tissue. *J Mol Cell Cardiol* 97: 82–92

Wijnker PJM, Sequeira V, Kuster DWD & van der Velden J (2019) Hypertrophic Cardiomyopathy: A Vicious Cycle Triggered by Sarcomere Mutations and Secondary Disease Hits. *Antioxid Redox Signal* 31: 318–358

Wilke CO (2020) cowplot: Streamlined Plot Theme and Plot Annotations for 'ggplot2'.

Wong AO-T, Wong G, Shen M, Chow MZ-Y, Tse WW, Gurung B, Mak SY, Lieu DK, Costa KD, Chan CW, *et al* (2019) Correlation between frataxin expression and contractility revealed by in vitro Friedreich's ataxia cardiac tissue models engineered from human pluripotent stem cells. *Stem Cell Res Ther* 10: 203

Xiao N (2018) ggsci: Scientific Journal and Sci-Fi Themed Color Palettes for 'ggplot2'.

Xie Y (2021) Knitr: A General-Purpose Package for Dynamic Report Generation in R.

Yao P & Fox PL (2013) Aminoacyl-tRNA synthetases in medicine and disease. *EMBO Mol Med* 5: 332–343

Yaplito-Lee J, Weintraub R, Jamsen K, Chow CW, Thorburn DR & Boneh A (2007) Cardiac Manifestations in Oxidative Phosphorylation Disorders of Childhood. *J Pediatr* 150: 407–411

Yoon J-Y, Daneshgar N, Chu Y, Chen B, Hefti M, Vikram A, Irani K, Song L-S, Brenner C, Abel ED, *et al* (2022) Metabolic rescue ameliorates mitochondrial encephalo-cardiomyopathy in murine and human iPSC models of Leigh syndrome. *Clin Transl Med* 12: e954

Zhang X, Li J, Zhang Y, Gao M, Peng T & Tian T (2022) AARS2-Related Leukodystrophy: a Case Report and Literature Review. *The Cerebellum*

Zhou W, Bos JM, Ye D, Tester DJ, Hrstka S, Maleszewski JJ, Ommen SR, Nishimura RA, Schaff HV, Kim CS, *et al* (2019) Induced Pluripotent Stem Cell–Derived Cardiomyocytes from a Patient with MYL2-R58Q-Mediated Apical Hypertrophic Cardiomyopathy Show Hypertrophy, Myofibrillar Disarray, and Calcium Perturbations. *J Cardiovasc Transl Res*

# EXPANDED VIEW FIGURE LEGENDS

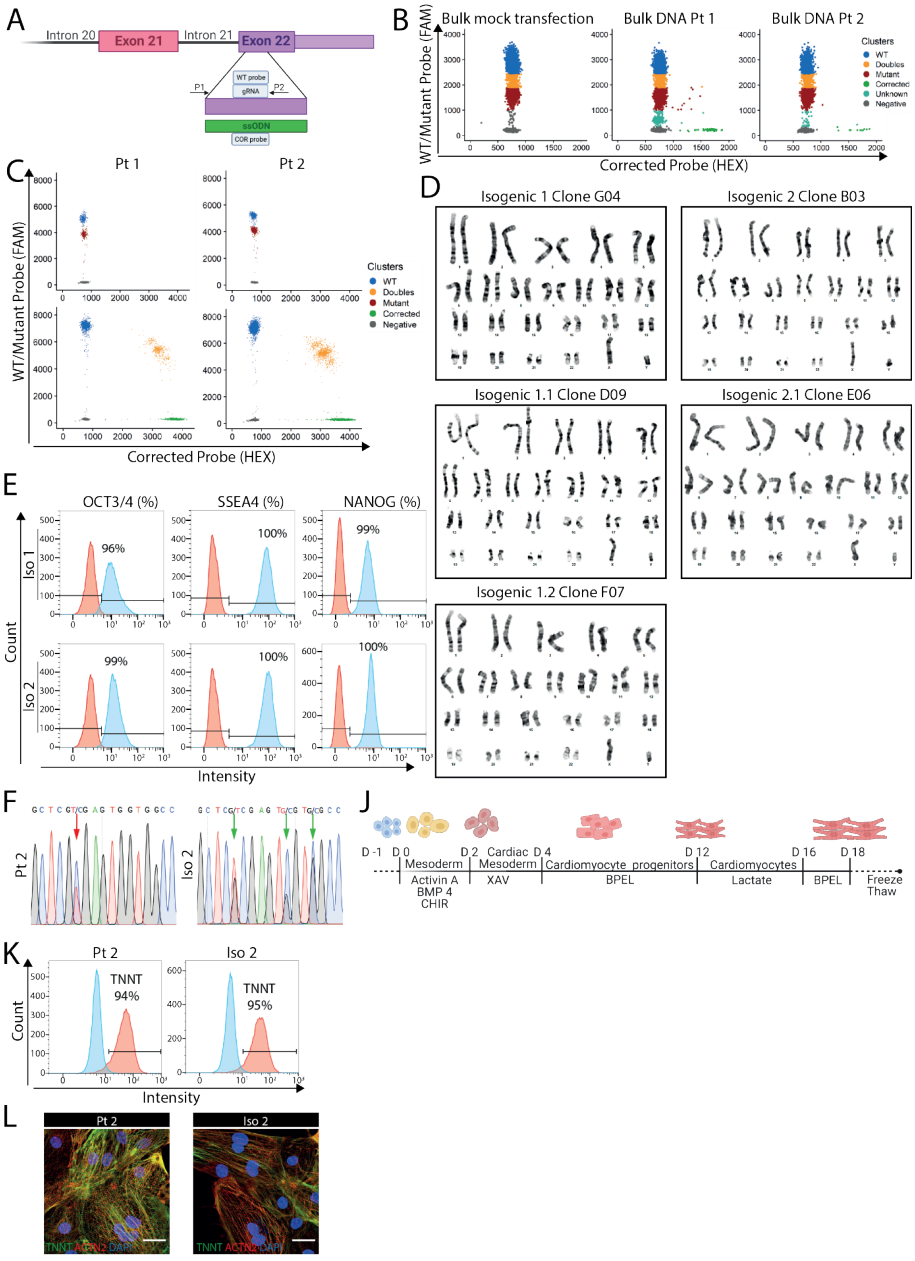


***Figure S1. Genetic correction in hiPSCs and differentiation into cardiomyocytes.***
A) Schematic representation for the CRISPR/Cas9 correction of the AARS2 c.2872C>T mutation and the screening

approach. The gRNA is uniquely complementary to the mutated allele. The WT probe binds to the WT allele with higher affinity than to the mutant allele. The COR probe binds uniquely to DNA matching the donor ssODN. P1 = forward primer 1, P2 = reverse primer 2, used for the screening. B) Screening of the transfected bulk hiPSC population. Mock transfection was performed without Cas9 protein but with the gRNA. WT droplets (blue) contain only the WT allele(s). Mutant droplets (red) contain only mutant allele(s). Mixed droplets (orange) contain one or multiple copies of both WT and mutant alleles. Corrected droplets (green) contain corrected alleles by homologous directed repair. Unknown droplets (turquoise) contain either unsuccessful PCR reactions or mutated alleles that underwent non-homologous end joining and therefore contained indels. Negative droplets (grey) do not contain any DNA. C) Screening of the hiPSC-clones grown from single-cell deposition from the bulk populations. The absence of the mutant cluster and the presence of the corrected cluster indicate the successful correction of the c.2872C>T mutation. D) Karyotypes from the targeted and corrected clone; Isogenic 1 clone G04 and Isogenic 2 clone B03 are Iso 1 and Iso 2, respectively. E) FACS analysis (histogram) of pluripotency markers OCT3/4, SSEA4 and NANOG (orange). Cells stained with isotype-matched antibodies were used as a negative control (blue). F) Sanger sequencing chromatogram of DNA isolated from Pt 2 and Iso 2 hiPSCs showing that the c.2872C>T mutation was corrected in Iso 2. G) Representative FACS analysis (histograms) of cardiac troponin (red) expression in Pt 2 and Iso 2 hiPSC-CMs after lactate selection. In blue, as a control the same cells were stained with isotype-matched antibodies. H) Immunofluorescence images from Pt 2 and Iso 2 hiPSC-CMs for TNNT2 (green), α-actinin-2 (ACTN2, red). Nuclei were stained in blue with DAPI, scale bar = 25 µm.

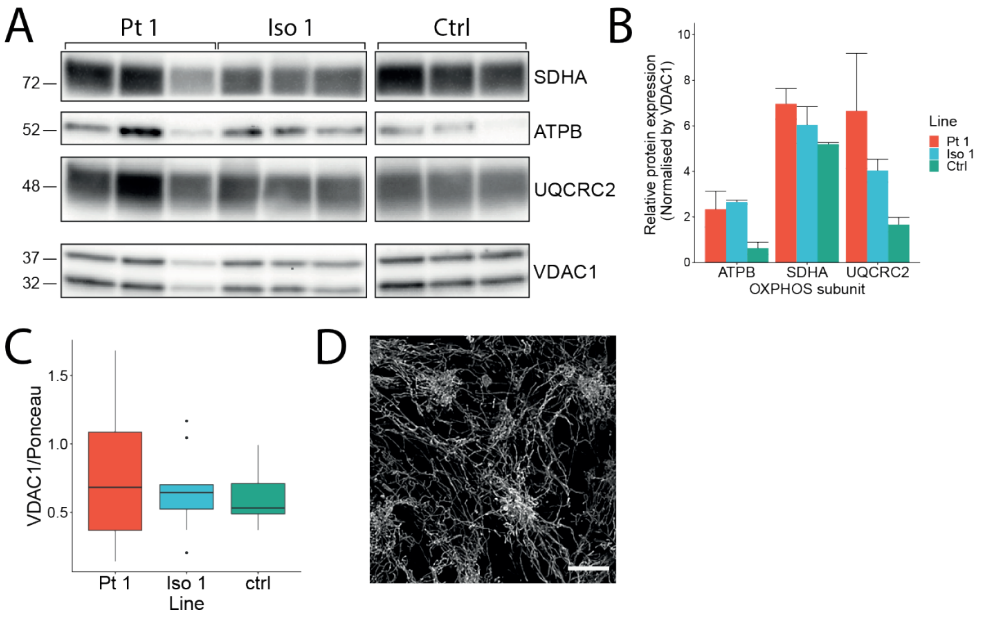


***Figure S2. Mitochondrial proteins and mitochondria network analysis.***
A) Western blot showing expression of the mitochondrial protein subunits SDHA, ATPB, UQCRC2 and VDAC1 in Pt 1, Iso 1 and Ctrl hiPC-CMs. Each column represents an independent differentiation (biological replicate, n = 3). B) Densitometric quantification (ADU: arbitrary units) of mitochondrial protein expression normalised to VDAC1 as a marker for total mitochondrial biomass. Data shown as mean with standard error. C) Expression of mitochondrial membrane porin VDAC1 normalised against total lysate protein assessed using Ponceau staining. D) Representative image of hiPSC-CMs where mitochondria were stained with the TMRM dye. Scale bar = 10 µm.

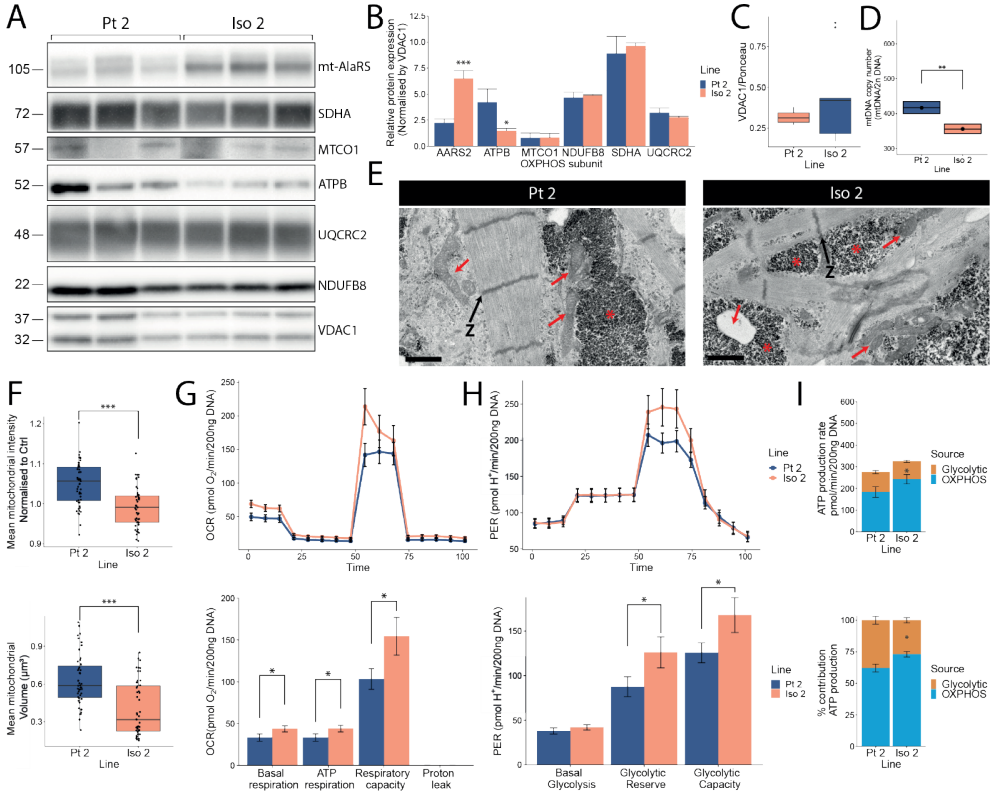


***Figure S3. Mitochondrial protein expression, mitochondrial organisation and metabolic flux in Pt 2 hiPSC-CMs.***

A) Western blot showing expression of the mitochondrial proteins mt-AlaRS, SDHA, MTCO1, ATPB, UQCRC2, NDUFB8 and VDAC1 in Pt 2 and Iso 2 hiPSC-CMs. Each column represents a single differentiation (biological replicate, n = 3). B) Densitometric quantification of mitochondrial protein expression normalised to VDAC1 expression as a marker for total mitochondrial biomass. C) Expression of mitochondrial membrane porin VDAC1 normalised against total lysate protein assessed using Ponceau staining as a quantification for mitochondrial biomass corrected for total biomass. D) mtDNA copy number per cell, quantified by ddPCR. The plot represents the Poisson minimum, mean, and maximum number of mtDNA per 2N nDNA copy number. Calculations based on Poisson distribution. N = 26, n = 4 biological repeat, ** P < 0.01, *** P < 0.001, Poisson statistics. E) transmission electron microscopy (TEM) images from Pt 2 and Iso 2 hiPSC-CMs, scale bar = 1 µm. F) Quantification of the intensity of the TMRM dye in mitochondria, normalised to the mean of the Ctrl and mean volume of each identified mitochondria. Each dot represents the mean value obtained per microscope field. N = 51, n = 3 biological repeat. G-H) Traces of extra-cellular flux assays in hiPSC-CMs by Seahorse measuring Oxygen consumption rate (OCR) (G) and proton extrusion rate (PER) (H). At the bottom of each panel, quantification of the different processes (basal respiration, ATP respiration, respiratory capacity, proton leak, (G, bottom) and basal glycolysis, glycolytic reserve, and glycolytic capacity (H, bottom)) is shown as a bar graph. N ≥ 18, n = 3-4 biological repeats. I) Total ATP production (top) and contribution of OXPHOS and glycolysis to total ATP production (bottom), calculated based on extra-cellular flux measurements. Statistical differences are denoted in comparison to Pt 2. n = 3-4 biological repeats. All data shown are mean with standard error. Statistics were indicated as follows unless otherwise indicated. * P < 0.05, ** P < 0.01, *** P < 0.001 with student's t-test.

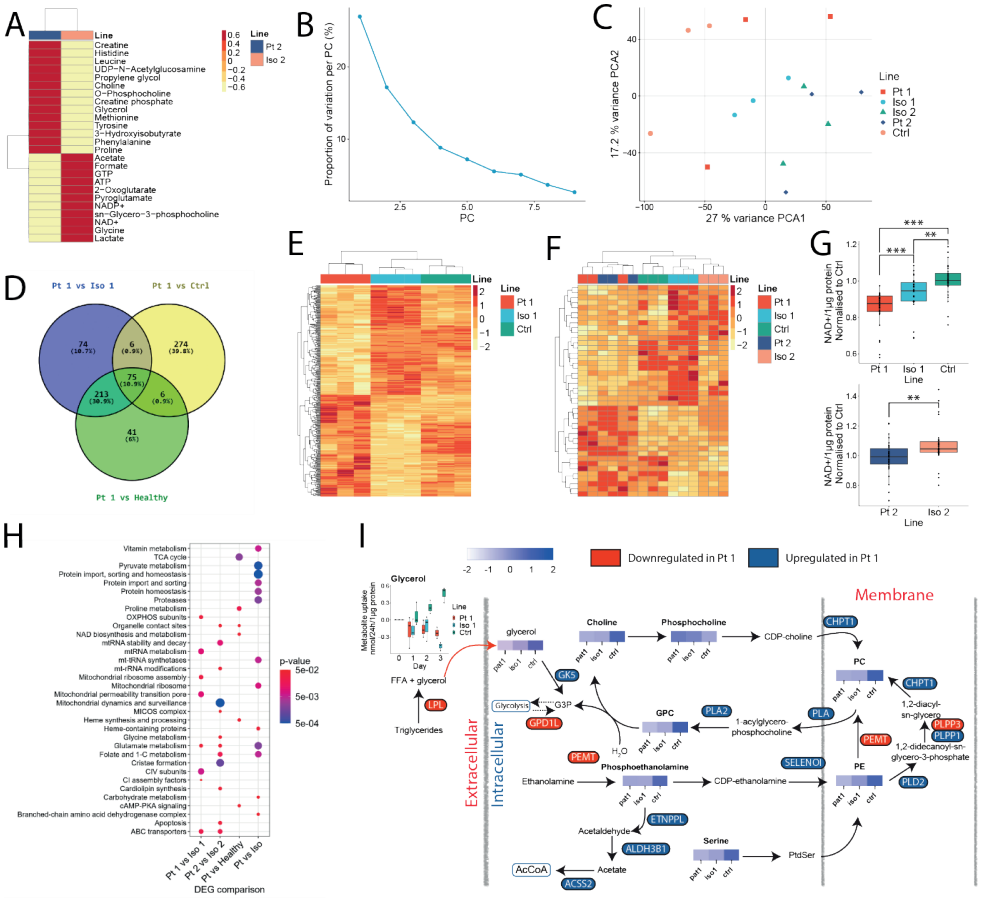


***Figure S4. Transcriptomics and metabolomics in hiPSC-CMs.***

A) Heatmap Hierarchical clustering of intra-cellular metabolites quantified by NMR (n = 3 biological repeats). The scale represents Z-score. B) Proportion of variance of all samples per principal component (PC) from bulk transcriptomics analysis. C) Scatter plot of PC1 and PC2 performed on hiPSC-CMs derived from all 5 lines. n = 3 biological repeats. D) Venn diagram portraying the total number (and percentages) of differentially expressed genes (DEGs) found by comparing Pt 1 with either Iso 1 (368 DEGs) or Ctrl (335 DEGs) or as a combined analysis of Pt 1 vs healthy (representing Iso 1 and Ctrl) (361 DEGs). E) Hierarchical clustering of the 361 DEGs from the Pt 1 vs healthy comparison. The scale represents Z-score. F) Hierarchical clustering of the 42 DEGs identified when comparing both patients against both isogenic lines. The scale represents Z-score. G) Pathway analysis on genes related to mitochondrial function from the MitoCata 3.0 atlas (p-value < 0.05). Each  H) Combined pathway analysis of intracellular metabolites; upregulated genes (blue) and downregulated (red) genes in Pt 1 versus Iso 1 and Ctrl hiPSC-CMs are visualised (p-value < 0.15 and 20% altered fold-change).

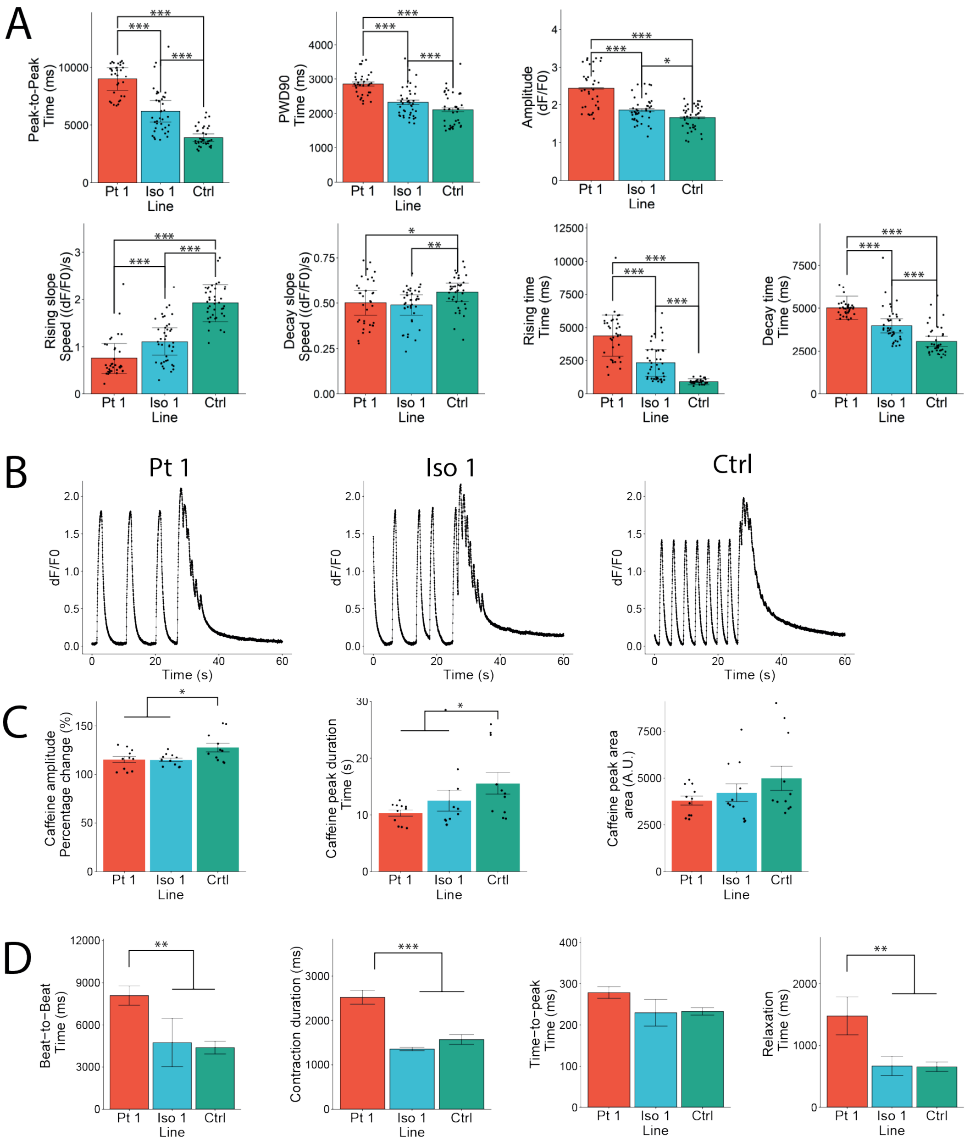


***Figure S5. Quantitative analysis of calcium transients and contraction properties.***

A) Analysis of rhythmic calcium transients showing peak-to-peak time, calcium transient width duration at 90% decay (PWD90), amplitude, rising slope, decay slope, rising time and decay time. Fluorescent amplitude was normalised using average background signal. Each dot represents the average of all calcium traces from a single well. N ≥ 35, n = 3 biological repeats. B) Representative traces showing calcium release from the sarcoplasmic reticulum upon the addition of 50 mM caffeine. C) Quantification of the caffeine-induced calcium release transient, amplitude change calculated over normal average amplitude, caffeine peak duration as PWD90, and area under the curve for the PWD90 duration. Each dot represents one well and analysed peak, N = 11, n = 3 biological repeats. D) Contraction analysis. All data shown are mean with standard error N ≥ 6 and n = 3 biological repeats.

All data shown are mean with standard error. Statistics indicated as follows, unless otherwise indicated. * $P < 0.05$, ** $P < 0.01$, *** $P < 0.001$ with student's t-test.

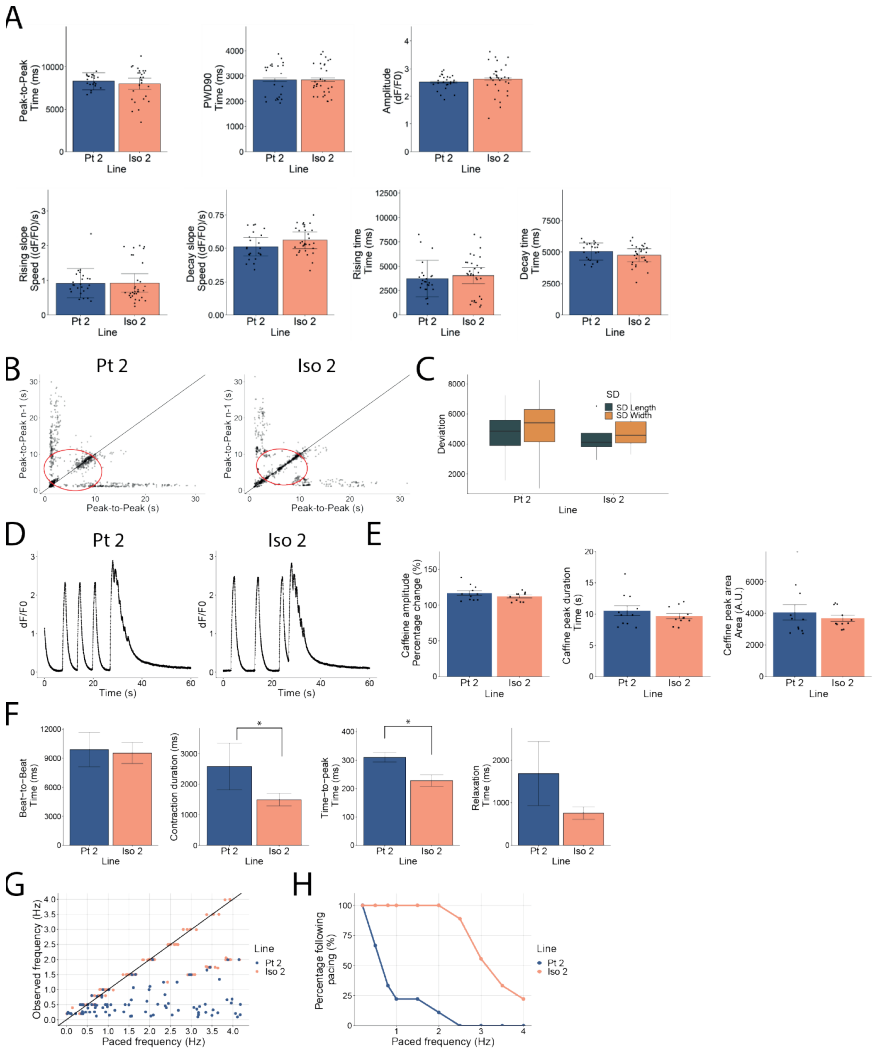


***Figure S6. Calcium and contractile analysis of Pt 2 and Iso 2.***

A) Analysis of rhythmic calcium transients in spontaneous contracting hiPSC-CMs showing peak-to-peak time, calcium transient width duration at 90% decay (PWD90), amplitude, rising slope, decay slope, rising time and decay time. Fluorescent amplitude normalised using average background signal. Each dot represents the average of all calcium traces from a single well. N ≥ 25, n = 4 biological repeats. B) Poincaré plots showing arrhythmia, marked as a red ellipse that was drawn based on calculating standard deviation along and perpendicular to the dissecting line. N = 60, n = 4 biological repeats. C) Quantification of the standard-deviation statistics used to generate the ellipse. D) Representative traces showing calcium release from the SR upon addition of 50 mM caffeine. E) Quantification of the caffeine-induced calcium release transient, induced amplitude change calculated based on average calcium transient amplitude, caffeine peak duration as PWD90 and area under the curve for the PWD90 duration. Each dot represents one well and analysed peak, N = 11, n = 3 biological repeats. F) Contraction analysis showing beat-to-beat time, total contraction duration, time-to-peak and relaxation time. N = 9, n = 3 biological repeats. G) Ability of hiPSC-CMs to follow increasing pacing frequencies. The x-axis shows paced frequency, the y-axis shows the observed beating rate of

the hiPSC-CMs. All dots underneath the intersecting line reflect hiPSC-CMs not contracting at the paced frequency. (N = 9, n = 3 biological repeats). H) Quantification of the percentage of samples able to follow the paced frequency up to 4 Hz. All data shown are mean with standard error and n = 3 biological repeats. Statistics indicated as follows, * P < 0.05, ** P < 0.01, *** P < 0.001 with student's t-test.

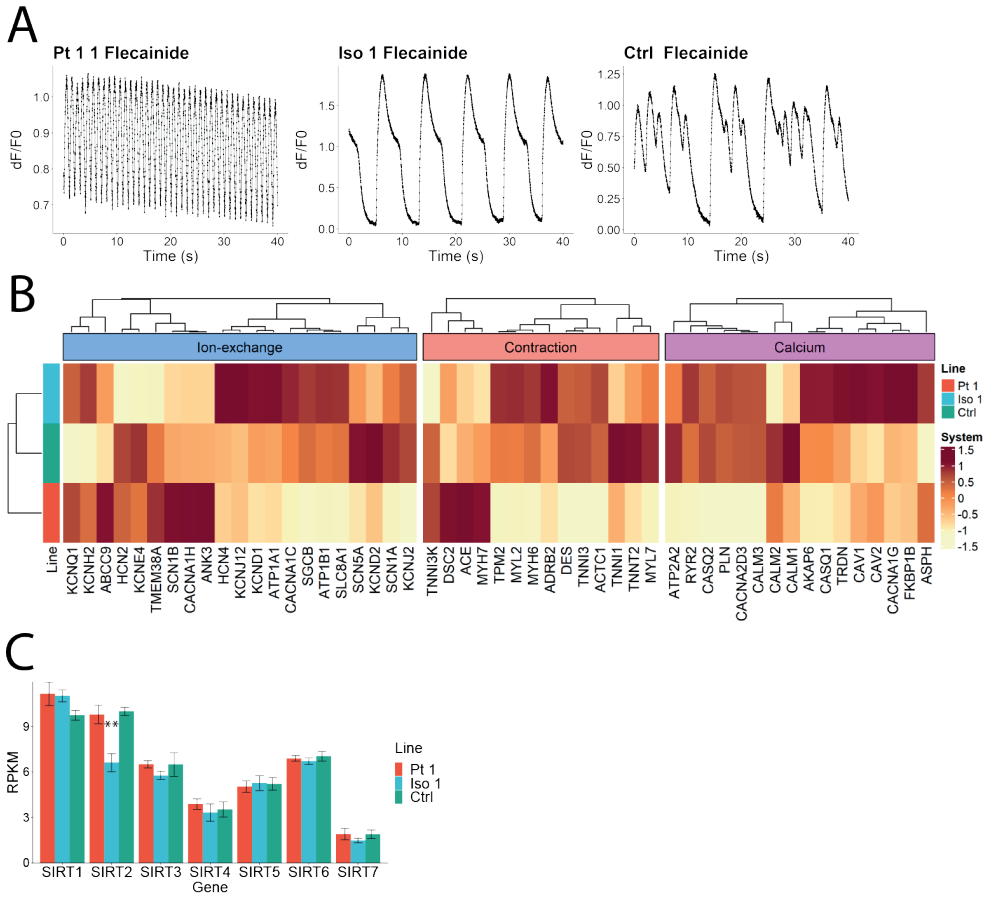


***Figure S7. Decreased sensitivity to Flecainide in Pt1, with altered expression profiles in ion-exchange, contraction and calcium related genes, but not in Sirtiuns.***

A) Representative traces showing calcium transients of hiPSC-CMs being paced at 1 Hz and exposed to 15 µM flecainide. B) Heatmap showing a curated list of genes based on KEGG and GO pathways related to ion exchange (blue), cardiomyocyte contraction (pink) and calcium homeostasis (purple). Final selection based on either p-value < 0.05 altered regulation versus Pt 1 or manually curated key genes. C) Expression of all sirtuin genes from transcriptomic data-analysis. Expression indicated as RPKM, n = 3 biological repeats.

All data shown are mean with standard error. Statistics indicated as follows, unless otherwise indicated. * P < 0.05, ** P < 0.01, *** P < 0.001 with student's t-test.